AGU PUBLICATIONS

JGR

Journal of Geophysical Research: Oceans

RESEARCH ARTICLE

10.1002/2014JC010115

Key Points:
- Interpretation of near-inertial currents using slab layer and two Ekman models
- Use of numerical model outputs to evaluate the observed near-inertial currents
- Scales of directly wind-forced near-inertial surface currents

Correspondence to:
S. Y. Kim,
syongkim@kaist.ac.kr

Citation:
Kim, S. Y., P. M. Kosro, and A. L. Kurapov (2014), Evaluation of directly wind-coherent near-inertial surface currents off Oregon using a statistical parameterization and analytical and numerical models, *J. Geophys. Res. Oceans*, *119*, 6631–6654, doi:10.1002/2014JC010115.

Received 13 MAY 2014
Accepted 20 AUG 2014
Accepted article online 26 AUG 2014
Published online 7 OCT 2014

Evaluation of directly wind-coherent near-inertial surface currents off Oregon using a statistical parameterization and analytical and numerical models

Sung Yong Kim[1], P. Michael Kosro[2], and Alexander L. Kurapov[2]

[1]Division of Ocean Systems Engineering, School of Mechanical, Aerospace, & Systems Engineering, Korea Advanced Institute of Science and Technology, Daejeon, Republic of Korea, [2]College of Earth, Ocean, and Atmospheric Sciences, Oregon State University, Corvallis, Oregon, USA

Abstract Directly wind-coherent near-inertial surface currents off the Oregon coast are investigated with a statistical parameterization of observations and outputs of a regional numerical ocean model and three one-dimensional analytical models including the slab layer, Ekman, and near-surface averaged Ekman models. The transfer functions and response functions, statistically estimated from observed wind stress at NDBC buoys and surface currents derived from shored-based high-frequency radars, enable us to isolate the directly wind-forced near-inertial surface currents. Concurrent observations of the wind and currents are crucial to evaluate the directly wind-forced currents. Thus, the wind stress and surface current fields obtained from a regional ocean model, which simulates variability of the wind and surface currents on scales comparable to those in observations, are analyzed with the same statistical parameterization to derive the point-by-point transfer functions and response functions. Model and data comparisons show that the regional ocean model describes near-inertial variability of surface currents qualitatively and quantitatively correctly. The estimated response functions exhibit decay time scales in a range of 3–5 days, and about 40% of the near-inertial motions are explained by local wind stress. Among the one-dimensional analytical models, the near-surface averaged Ekman model explains the statistically derived wind-current relationship better than other analytical models.

1. Introduction

Near-inertial oscillations observed ubiquitously in the ocean are mainly caused by spatially and temporally varying wind stress, particularly, related to moving storms and fronts with time scales of a day or two [e.g., *Pollard and Millard*, 1970; *D'Asaro*, 1985]. However, in some cases the timings between wind forcing and wind-forced near-inertial responses are not well matched. It has been unclear how to distinguish the near-inertial motions directly forced by local wind stress from near-inertial energy either generated elsewhere or propagated into the region and how to quantify their temporal and spatial characteristics.

Specifically, the near-inertial currents (oscillations) are excited by either continuous broadband wind stress or impulsive wind stress imposed on the ocean at rest. Those driving forces contain nonzero energy in near-inertial frequency band [e.g., *Crawford and Large*, 1996; *Elipot and Gille*, 2009; *Kim and Kosro*, 2013]. In order to investigate the directly wind-forced near-inertial surface currents, the wind and current data are required to have similar and appropriate resolutions in time and space. As direct measurements of wind stress and currents are limited in either space or time, it has been difficult to investigate the directly wind-forced near-inertial currents. Simulations using comprehensive high-resolution models forced by spatially and temporally varying winds can provide an additional opportunity to estimate the ocean response in the near-inertial frequency band.

As a dynamical framework to explain wind-forced near-inertial oscillations, the slab layer model has been widely used [e.g., *Pollard and Millard*, 1970; *D'Asaro*, 1985; *Alford*, 2001]:

$$\frac{\partial \mathbf{u}}{\partial t} + if_c\mathbf{u} + r\mathbf{u} = \frac{\boldsymbol{\tau}^w}{\rho h}, \tag{1}$$

where f_c, ρ, r, and h denote, respectively, the inertial frequency, the water density, the damping coefficient ($r > 0$, $r \ll f_c$), and the mixed layer depth. The individual components in currents ($\mathbf{u}$) and wind stress ($\boldsymbol{\tau}^w$) are combined into the complex numbers, i.e., $\mathbf{u} = u + iv$ and $\boldsymbol{\tau}^w = \tau_x^w + i\tau_y^w$.

Based on assumptions of infinite viscosity within the surface mixed layer and of zero viscosity below that, wind stress and currents within the mixed layer are hypothesized to be orthogonal (e.g., *D'Asaro* [1985], see equations (1) and (3)). However, in the comparison between analytical solutions and observations, the data-derived wind-current relationship is not always consistent with the slab layer model implementation in terms of its phase and the influence of stratification and viscosity [e.g., *Gonella*, 1972; *Daniault et al*., 1985; *Paduan et al*., 1989; *Weller and Plueddemann*, 1996; *Ralph and Niiler*, 1999]. Moreover, *Pollard and Millard* [1970]; *Kundu* [1976]; and *Weller* [1982] acknowledged the limitations of the slab layer model for simulating the observed phenomena such as mixing due to passing storms. On the other hand, the Ekman model [*Ekman*, 1905] describes the currents driven by a steady wind under a constant viscosity within the Ekman layer as a downward spiral with magnitudes decreasing to zero with depth and a veering of 45° at surface and 225° at the bottom of the layer to the right of wind direction in the northern hemisphere [e.g., *Krauss*, 1972; *Csanady and Shaw*, 1980]. *Gonella* [1972] expanded the Ekman model into the wind-current responses at all frequencies using the Ekman model. The extended Ekman model with a damping term (r in equation (2)) is given as

$$\frac{\partial \mathbf{u}}{\partial t} + if_c\mathbf{u} + r\mathbf{u} = \frac{1}{\rho}\frac{\partial \boldsymbol{\tau}}{\partial z}, \tag{2}$$

where $\boldsymbol{\tau}$ is the internal stress in the boundary layer.

For the interpretation of wind-forced near-inertial motions, the Ekman model has been less frequently used compared with the slab layer model. However there were several studies describing the wind-current system under idealized vertical viscosity profiles and stratified/unstratified water columns using the Ekman model [e.g., *Madsen*, 1977; *Lewis and Belcher*, 2004; *Elipot and Gille*, 2009; *Price and Sundermeyer*, 1999].

In this study, we address four questions: (1) what are the characteristics of the directly wind-coherent near-inertial surface currents? (2) which analytic model best explains the near-inertial surface currents? (3) are we justified in using spatially limited wind observations in estimates of directly wind-forced near-inertial (surface) currents? and (4) how well does a coastal ocean model reproduce the near-inertial signal of surface currents in a statistical sense?

To address these questions, we examine the directly wind-coherent near-inertial surface currents and their temporal and spatial scales using transfer functions estimated from local winds and surface currents, which are obtained from observations and realistic numerical model simulations. The observational resources for this paper are the high resolution (6 km in space and hourly in time) coastal surface currents measured by an array of high-frequency radars (HFRs) and the coastal winds at NDBC buoys off Oregon and southern Washington [e.g., *Kosro*, 2005; *Kim and Kosro*, 2013]. Although *Kim et al*. [2009, 2010] already provided the detailed analysis and interpretations of the wind transfer function, the near-inertial currents were not clearly delineated in previous studies because inertial energy off San Diego, California ($f_c = 1.07$ cycles per day (cpd)) in those studies is relatively low and overlaps with variance of the diurnal wind and tides. Here we choose the Oregon coast as a study domain where near-inertial variance is clearly separated from tides (K_1 and M_2) and has a high signal-to-noise ratio (SNR). Furthermore, high-resolution numerical simulation outputs are available to examine the wind-current system in this region.

This paper is organized as follows. First, we review three one-dimensional analytical models including the slab layer, Ekman, and near-surface averaged Ekman models and compare their analytical solutions that present the directly wind-forced responses (section 2). Then, the observed and modeled surface current maps and wind fields are compared in terms of their energy spectra and temporal and spatial decorrelation scales in near-inertial frequency band (section 3). In section 4, the data-derived and model-derived transfer functions and response functions are compared; a statistical parameterization using a linear regression between wind stress and surface currents will be used to evaluate which of the three analytical models best explains the directly wind-coherent near-inertial motions and quantifies their scales in time and space. Finally, concluding remarks follow in section 5.

2. Analytical Models

In order to examine the directly wind-forced inertial motions, we adopt the approach using the transfer function and response function that connect the wind stress and currents with a linear (or nonlinear)

relationship in the frequency (σ) and time (t) domains, respectively [e.g., *Kim et al.*, 2009]. Here we review the transfer function and response function (see definitions below) from three analytical models.

2.1. Slab Layer Model

Pollard and Millard [1970] proposed a single layer model that describes current responses to the wind in the upper ocean, implemented with a friction term (r in equation (1)) to account for the time decay of inertial motions. In order to implement vertical mixing driven by moving storms and fronts, the water column has been modeled with infinite viscosity within the mixed layer and zero viscosity below the layer. The transfer function ($\mathbf{H_S}$) in the slab layer model, as corrected from *D'Asaro* [1985], is shown to be

$$\mathbf{H_S}(\sigma)=\frac{\hat{\mathbf{u}}(\sigma)}{\hat{\tau}(\sigma)}=\frac{1}{\rho h[i(\sigma+f_c)+r]}, \tag{3}$$

where $\hat{\mathbf{u}}$ and $\hat{\tau}$ are the Fourier coefficients of currents and wind stress, respectively.

The corresponding response function ($\mathbf{G_S}$) in the time domain is the inversely Fourier transformed transfer function (see *Csanady and Shaw* [1980] or Appendix A1 for more details).

$$\mathbf{G_S}(t)=\frac{1}{2\pi}\int_{-\infty}^{\infty}\mathbf{H_S}(\sigma)e^{i\sigma t}\mathrm{d}\sigma, \tag{4}$$

$$=\frac{1}{2\rho h}e^{-if_c t}e^{-rt}. \tag{5}$$

In general, $\mathbf{G}$ is a function of vertical coordinate z and time t (z is positive upward). For the slab layer model, $\mathbf{G}$ is independent of z. By definition, the wind-driven current response is the time convolution of the response function and wind stress at a single location:

$$\mathbf{u}(z,t)=\int_0^t\mathbf{G}(z,t-t')\boldsymbol{\tau}(t')\mathrm{d}t'. \tag{6}$$

When the wind stress corresponding to a passing storm at the time α is given by a delta function, $\boldsymbol{\tau}(t')=\delta(t'-\alpha)$ ($\alpha>0$), the response function itself becomes the current response, which corresponds to the hypothesis of the random storm timing in *D'Asaro* [1985]:

$$\mathbf{u}(z,t)=\mathbf{G}(z,t-\alpha). \tag{7}$$

The damping parameter (r) in the slab model is introduced to represent the loss of mixed layer energy to downward propagating motions. Without this, the inertial current response to random storms would increase proportionally to $\sqrt{t}$ similar to the random walk model [e.g., *Kundu et al.*, 1983; *Kundu*, 1984]. The damping factor is chosen to be $0<r\ll f_c$. A constant ratio (r/f_c) has been recommended in the studies of the inertial energy distribution at global and basin scales [e.g., *Alford*, 2001]. The inverse of the damping term (r^{-1}) is the decay time scale of wind-forced oscillations.

2.2. Ekman Model

Ekman [1905] proposed an analytical model to describe the ocean responses to wind stress, including the vertical spiral under the steady wind stress conditions and time-dependent inertial oscillations. Based on the Ekman theory, the transfer function ($\mathbf{H_E}$) has been derived under assumptions of the infinite depth and depth-independent viscosity (ν):

$$\mathbf{H_E}(z,\sigma)=\frac{\hat{\mathbf{u}}(z,\sigma)}{\hat{\tau}(\sigma)}=\frac{e^{\lambda z}}{\lambda\rho\nu}, \tag{8}$$

where $\lambda=\sqrt{[i(\sigma+f_c)+r]/\nu}$ [e.g., *Gonella*, 1972; *Krauss*, 1972; *Lewis and Belcher*, 2004; *Wang et al.*, 2001; *Kim et al.*, 2009]. The response function ($\mathbf{G_E}$) is (Appendix A2 for more details),

$$\mathbf{G_E}(z,t)=\frac{1}{2\pi}\int_{-\infty}^{\infty}\mathbf{H_E}(z,\sigma)e^{i\sigma t}\mathrm{d}\sigma, \tag{9}$$

$$=\frac{1}{\rho\sqrt{\pi\nu t}}e^{-\frac{z^2}{4\nu t}}e^{-if_c t}e^{-rt}. \tag{10}$$

Csanady and Shaw [1980] highlighted that the vertical extent of the Ekman layer is proportional to $\sqrt{2\nu/f_c}$ and the time decay of inertial oscillations in the initial state primarily depends on $(\nu t)^{-1/2}$ rather than e^{-rt}

(compare equation (5) and equation (10)). When the inertial motions are interpreted with the Ekman model, the damping term (e^{-rt}) may not be well determined in the inverse estimates as it is a secondary term (see sections 2.4 and 4.2). *Krauss* [1972] presented analytical solutions for near-inertial currents with the finite depth Ekman model. Moreover, time-transient Ekman models have been investigated elsewhere [e.g., *Gonella*, 1971; *Lewis and Belcher*, 2004], and their solutions derived from the Fourier and Laplace transforms are found to be identical (Appendix A2). The wind transfer functions under depth-dependent viscosity had been extensively examined elsewhere [e.g., *Madsen*, 1977; *Lentz*, 1995; *Elipot and Gille*, 2009; *Price and Sundermeyer*, 1999; *McWilliams et al.*, 2009].

2.3. Near-Surface Averaged Ekman Model

As HFR-derived surface currents are composed of currents averaged over the upper $O(1)$ m depth [e.g., *Stewart and Joy*, 1974; *Barrick et al.*, 1977], we suggest that the transfer function ($\mathbf{H}_\mathbf{E}^*$) and response function ($\mathbf{G}_\mathbf{E}^*$) be averaged from surface to depth z^*:

$$\mathbf{H}_\mathbf{E}^*(\sigma) = \frac{1}{z^*}\int_0^{z^*} \mathbf{H}_\mathbf{E}(z,\sigma)\,\mathrm{d}z, \tag{11}$$

$$= \frac{1}{z^*}\frac{1}{\lambda^2\rho\nu}\left(e^{\lambda z^*}-1\right), \tag{12}$$

and

$$\mathbf{G}_\mathbf{E}^*(t) = \frac{1}{z^*}\int_0^{z^*} \mathbf{G}_\mathbf{E}(z,t)\,\mathrm{d}z, \tag{13}$$

$$= \frac{1}{\rho z^*}\mathrm{erf}\left(\frac{z^*}{\sqrt{4\nu t}}\right)e^{-if_c t}e^{-rt}, \tag{14}$$

respectively, where

$$\mathrm{erf}(x) = \frac{2}{\sqrt{\pi}}\int_0^x e^{-t^2}\mathrm{d}t. \tag{15}$$

2.4. A Comparison of Analytical Models

The amplitudes and phases of the three transfer functions discussed above are compared in Figure 1, where the positive (negative) frequency along the horizontal axis corresponds to the counter-clockwise (clockwise) rotating currents. The amplitude has a peak and the phase is changed abruptly at the inertial frequency ($f_c = -1.40$ cpd) [e.g., *Gonella*, 1972]. The phase in the Ekman model (equation (8)) and near-surface averaged Ekman model (equation (12)) is shown to vary with the depth ($z = n\delta_E/4$) and the averaging depth ($z^* = n\delta_E/4$), respectively, where $n = 0$, 1, 2, 3, and 4 (Figures 1d and 1f). However, the phase in the slab layer model is always $\pm 90^\circ$ within the mixed layer (equation (3) and Figure 1b), meaning that the wind-driven currents within the mixed layer are in quadrature with the wind stress at all frequencies, which fails to explain the surface Ekman flow for the steady wind stress at 45° right of the wind direction.

The factors contributing to the time decay of near-inertial oscillations in individual response functions (equations (5), (10), and (14)) are compared in Figure 2. For consistency, the real parts of individual response functions are examined using the same damping coefficient ($r = 0.1f_c$). The Ekman and near-surface averaged Ekman models show rapidly decaying amplitudes at early time as opposed to slowly decaying pattern in the slab layer model. The time evolutions of e^{-rt}, $t^{-1/2}$, and their product ($e^{-rt}t^{-1/2}$) show that $t^{-1/2}$ is the primary decay term and e^{-rt} is the secondary decay term for near-inertial oscillations [e.g., *Lewis and Belcher*, 2004] (Figure 2). This modified Ekman transfer function should better represent HFR-derived wind-current relationships.

3. Observations and Numerical Simulations

3.1. Observations of Surface Currents and Winds

In this study, the HFR-derived hourly averaged surface currents and wind records at NDBC 46050 (W1), 46029 (W2) and 46041 (W3) buoys off Oregon and southern Washington for two years (2007–2008) are utilized [e.g., *Kosro*, 2005; *Kim and Kosro*, 2013]. The hourly and 6 km resolution maps of HFR surface currents

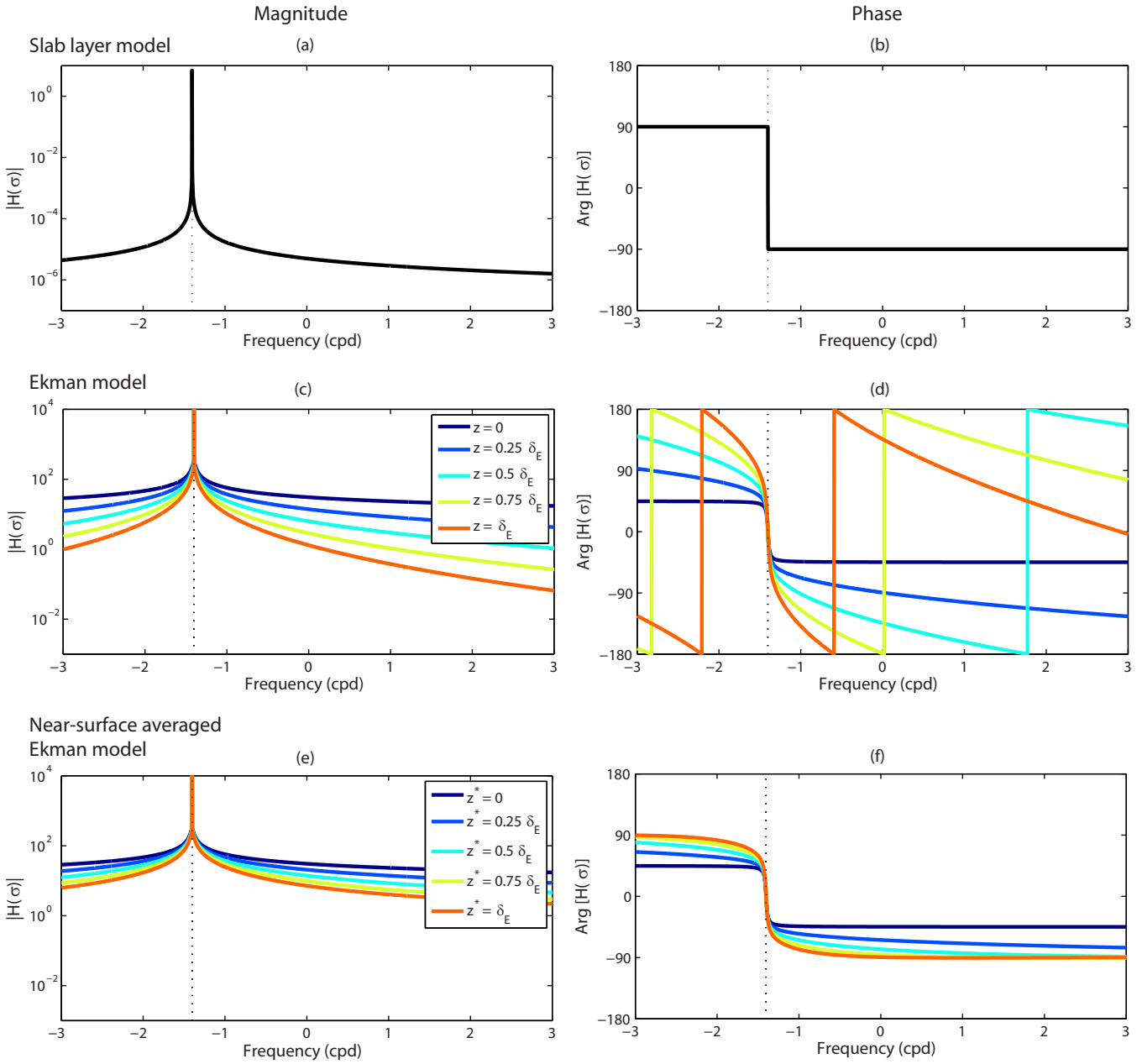

Figure 1. Transfer functions of (top) the slab layer model (middle) the Ekman model as a function of depth (z), and (bottom) the near-surface averaged Ekman model as a function of averaging depth (z^*). Their magnitudes ($kg^{-1}\ m^2\ s$) are on the left panels and phases (degrees) are on the right plots ($\nu = 1\times10^{-3}\ m^2\ s^{-1}$, $r = 1\times10^{-6}\ s^{-1}$, $h = 10\delta_E$, and $f_c = 1.40$ cpd at 44.49°N). Depths are chosen as each $0.25\delta_E$ increment from the surface to the Ekman depth (δ_E). The range of y axis in the magnitude plots (Figures 1a, 1c, and 1e) is the same.

are obtained by optimal interpolation of the radial velocity maps from an array of 11 HFRs (standard range and long range) along the Oregon coast (Figure 3b), and its effective spatial coverage (at least 90% data availability over two years) is shown as a yellow contour in Figure 3b. Note that only nine sites are visible as black dots in Figure 3b because the two sites (one long range and one standard range) at Yaquina Head are located close to each other and the southernmost site at Point St. George is below the southern boundary of Figure 3b.

3.2. A Numerical Model

The forward numerical simulations obtained with the regional ocean model provide the surface currents with hourly temporal and 2 km horizontal resolution for about one year (November 2008 to August 2009) (Kurapov A. L. et al., Sea surface temperature variability in the upwelling region off Oregon influenced by

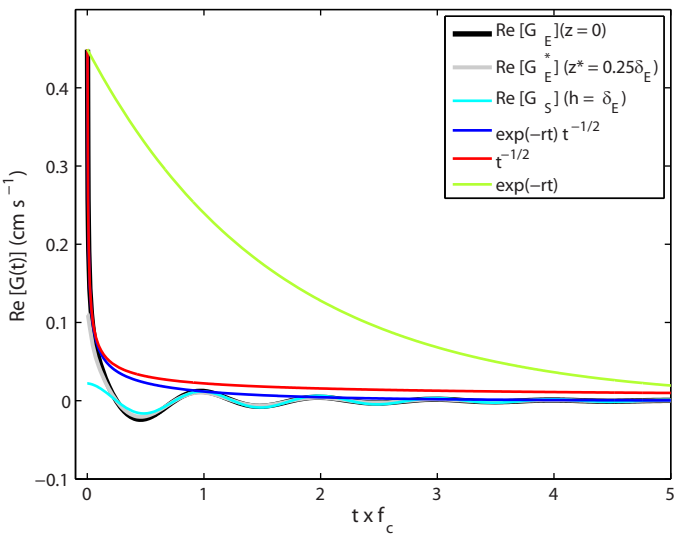

Figure 2. Comparison of the contribution of each term in surface current response: real part (u component) of the Ekman transfer function (Re[$\mathbf{G_E}(t)$]), the upper $0.25\delta_E$ averaged Ekman transfer function (Re[$\mathbf{G_E^*}(t)$]), the slab layer model transfer function (Re[$\mathbf{G_S}(t)$]) with $h=\delta_E$, the combined term ($e^{-rt}t^{-1/2}$), the time-transient term ($t^{-1/2}$), and the friction term (e^{-rt}) under assumptions of $\nu=1\times10^{-4}$ m^2 s^{-1}, $r=0.1f_c$, and $\delta_E=\pi\sqrt{2\nu/f_c}$.

the Columbia River plume, manuscript in preparation]. The model is based on the Regional Ocean Modeling System (ROMS), a free-surface, fully nonlinear, primitive equation model featuring terrain-following coordinates in the vertical, advanced numerical features [*Shchepetkin and McWilliams*, 2003, 2005], and a comprehensive subgrid vertical turbulence scheme [*Mellor and Yamada*, 1982]. The domain extends from 41°N to 50°N and from 130°W to coast (the black box in Figure 3a). Model resolution is 2 km in the horizontal and 40 terrain-following layers in the vertical, with relatively better resolution near the surface and bottom. Atmospheric forcing is obtained using bulk flux formulation [*Fairall et al*., 1996]. The required atmospheric fields (including the near-surface wind speed and direction, air pressure, incoming shortwave and long-wave radiation, relative humidity, air temperature, and cloud cover) are obtained from the National Oceanic and Atmospheric Administration North American Model (NOAA NAM), constrained by data assimilation. The atmospheric fields are provided at the 12 km spatial and 6 hourly temporal resolutions. Subtidal boundary conditions are obtained from the 1°/12th data assimilative Hybrid Coordinate Ocean Model (HYCOM),

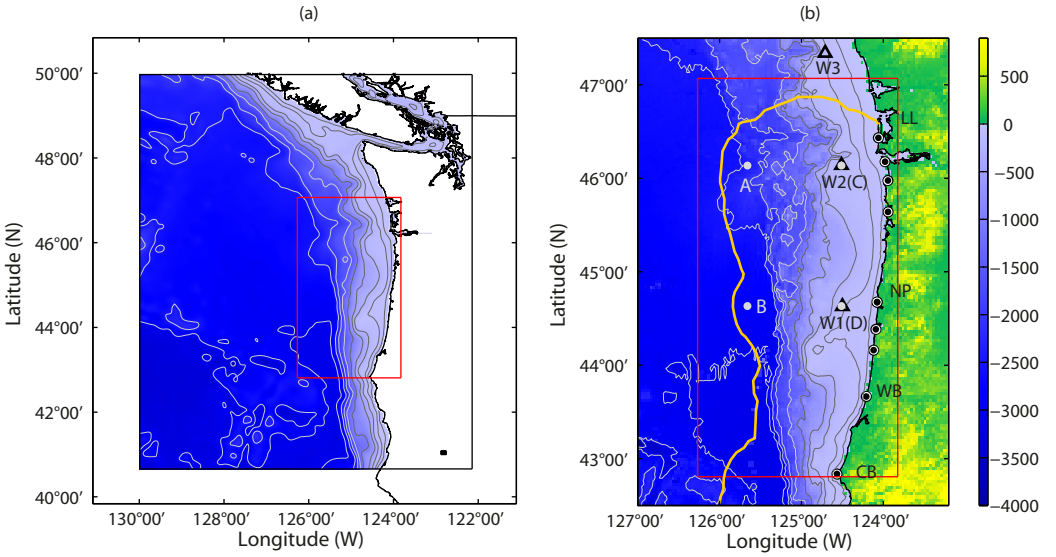

Figure 3. A study domain of directly wind-coherent near-inertial surface currents off Oregon and southern Washington. (a) A numerical model domain (black box). ROMS wind stress and surface currents with hourly and 2 km resolutions are analyzed. (b) A zoomed-in view of the Oregon coast. A yellow contour denotes the effective spatial coverage of HFRs, which denotes at least 90% data availability for two years. The black triangles and black-white dots on the coastline indicate NDBC wind buoys [46050 (W1), 46029 (W2), and 46041 (W3)] and an array of the HFR network, respectively. The bottom bathymetry is contoured with 50 m, 100 m, 250 m, 500 m, 1000 m, 1500 m, 2000 m, 2500 m, and 3000 m. The subsampled model domain is denoted with red boxes in Figures 3a and 3b. Four grid points (A, B, C, and D) are chosen to present the spatial coherence of the model wind stress and surface currents (Figure 3b). C and D correspond to the nearby grid points from W2 and W1 buoys, respectively. As a reference, major coastal regions are denoted by abbreviated two letter names from south to north: Cape Blanco (CB), Winchester Bay (WB), Newport (NP), and Loomis Lake (LL).

implemented by the US Navy. The HYCOM outputs have been provided as instantaneous fields once a day. The inertial motions are aliased in such a record, showing as strong oscillations in velocity fields with an approximately 2.8 day period. This signal has been removed from the HYCOM-derived boundary conditions using a 5 day half-amplitude low-pass filter. Barotropic tides are added at the open boundaries, using eight tidal constituents (M_2, S_2, K_1, O_1, K_2, N_2, P_1, and Q_1). Tidal constants corresponding to these are obtained from the 1°/30th resolution regional (US West Coast) shallow-water model TPXO 7.2 constrained by assimilation of satellite altimetry and in situ data [*Egbert and Erofeeva*, 2002]. Note that our ROMS implementation does not assimilate any observations.

The model simulation includes the Columbia River (CR) fresh water discharge. The seasonal peak comes in May to June. The 2 km resolution model provides only a crude approximation of the CR estuary, which is 6–8 km wide near the river mouth. Our model uses realistic geometry in the estuary over the distance of 15 km inland from the mouth and then the river is idealized as a straight channel of a constant depth. At the end of the river, at a distance of about 50 km from the river mouth, a flux of fresh water is specified using a time series of the daily averaged CR volume transport observed at the US Geological Survey Beaver Army station. The temperature data of the discharged water are not available at this station during our study period. Instead, the monthly temperature climatology obtained from a number of previous years at this station is used as the model input.

The wind speed at every point of the ROMS grid at every time step is obtained by linear interpolation in space and time. The model wind stress is computed internally by ROMS using the bulk flux formulation and wind velocity from NAM. For convenience in the data analysis, the model wind stress and surface currents saved by ROMS are spatially resampled at every third grid point. Then, the resulting hourly 6 km resolution maps of model wind stress and surface currents are analyzed. Considering the original 6 hourly temporal resolution of the NAM wind speed, the Nyquist frequency of the ROMS forcing is equal to 2 cycles per day (cpd), so the wind stress will be effective forcing on the near-inertial currents in the study domain.

A model subdomain for comparison with the HFR near-inertial surface currents is chosen (red boxes in Figures 3a and 3b) to enclose the area of the effective spatial coverage of HFRs. Four grid points (A, B, C, and D) are chosen for study of the spatial coherence of the model wind stress and surface currents (Figure 3b). C and D are the closest grid points to the W2 and W1 buoys, respectively.

3.3. Evaluation of Model Outputs

3.3.1. Preliminary Remarks

In this section, we will examine the spectral contents and length scales of the surface currents and wind data (wind stress) obtained from observations and numerical simulations, which can provide justification for the use of the model-derived wind transfer function in future analyses. For model evaluation, the spectral contents of ROMS surface currents and wind stress will be presented with the rotary energy spectra spatially averaged over the study domain (Figure 4). Their decorrelation time and length scales will be estimated with the decay slope of the near-inertial peak and the spatial coherence in the near-inertial frequency band (Figure 5), respectively, as conducted in *Kim and Kosro* [2013]. The coherence, the correlation within a specific frequency band, is a useful tool to examine the spatial structure of variability in a given frequency band [e.g., *Emery and Thomson*, 1997; *Kim and Kosro*, 2013]:

$$\hat{c}\left(\Delta\mathbf{x},\hat{f}_c\right)=\frac{\langle\hat{\boldsymbol{\xi}}(\mathbf{x},\hat{f}_c)\;\hat{\boldsymbol{\xi}}^{\dagger}(\mathbf{x}+\Delta\mathbf{x},\hat{f}_c)\rangle}{\sqrt{\langle|\hat{\boldsymbol{\xi}}(\mathbf{x},\hat{f}_c)|^2\rangle}\sqrt{\langle|\hat{\boldsymbol{\xi}}(\mathbf{x}+\Delta\mathbf{x},\hat{f}_c)|^2\rangle}}, \tag{16}$$

where $\hat{\boldsymbol{\xi}}$ is the Fourier coefficient of vector time series (currents or wind stress) and $\langle\cdot\rangle$ indicates averaging over the near-inertial frequency band ($\hat{f}_c$). Negative (positive) phases indicate that the reference physical variable at $\mathbf{x}$ leads (follows) the target physical variable at $\mathbf{x}+\Delta\mathbf{x}$.

The near-inertial frequency band ($\hat{f}_c$) in this paper (e.g., black boxes in Figures 4a and 4b) is defined as $f_c^+ \pm$ 0.15 cpd, where a reference frequency (f_c^+) is either the effective Coriolis frequency at a given location or the nearest frequency to the averaged value of inertial frequencies at two locations when the spatial coherence estimate is involved [see *Kim and Kosro*, 2013]. The effective Coriolis frequency is the sum of the planetary Coriolis frequency and the half of relative vorticity [e.g., *Kunze*, 1985].

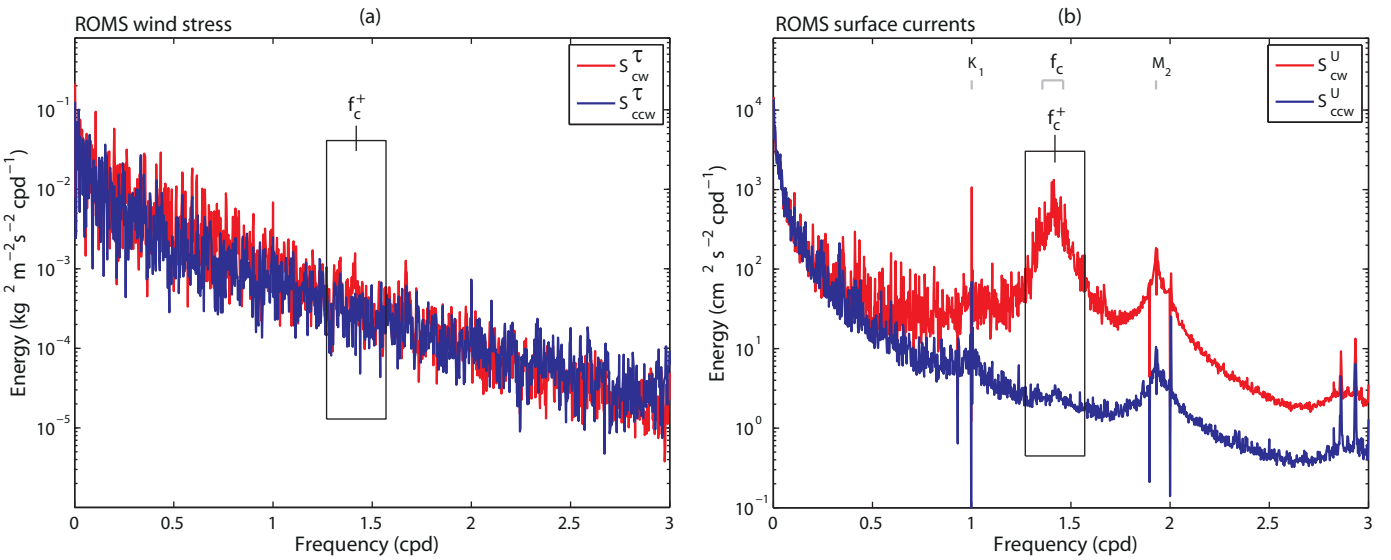

Figure 4. Spatially averaged rotary energy spectra of (a) ROMS wind stress and (b) ROMS surface currents. The clockwise and counter-clockwise energy spectra are presented with the red and blue colors, respectively. Black boxes centered by a reference frequency (f_c^+) denote the near-inertial frequency bands. The range of the local inertial frequency (f_c) in the study domain and major tidal frequencies (K_1 and M_2) are marked as gray lines in Figure 4b.

For the quantitative comparison between ROMS and HFR clockwise near-inertial surface currents, we present the probability density functions (PDFs) of their amplitudes (the left column of Figure 6) and decorrelation time and length scales (the middle and right columns of Figure 6). The PDFs are presented with values in the entire study domain (the top row in Figure 6), the along-shore averaged values and their standard deviation as a function of distance from the coast (the middle row in Figure 6), and the cross-shore averaged values and their standard deviation as a function of latitude (the bottom row in Figure 6).

3.3.2. Spectral Contents

The wind variability off the Oregon coast is dominated by alongshore fluctuations at both diurnal [e.g., *Perlin et al*., 2004] and subinertial time scales; the latter is the primary driver of circulation over the shelf. The standard deviation of alongshore wind stress is about three times higher than that of the cross-shore wind stress [e.g., *Smith*, 1968; *Halliwell and Allen*, 1987; *Samelson et al*., 2002; *Kim*, 2014].

The model wind stress has a red spectrum with relatively insignificant diurnal variance (Figure 4a) compared to the observed wind [e.g., *Kim*, 2014]. The spectrum of clockwise model surface currents contains the near-inertial variance, a sharp peak at the K_1 frequency, a cuspate peak at the M_2 frequency, and variance at harmonic frequencies of primary tidal constituents (a red curve in Figure 4b), which is comparable with the previously published observed energy spectra (see Figure 1b in *Kim and Kosro* [2013]). The variance of model surface currents in the counter-clockwise near-inertial frequency band is nearly the noise level of the spectrum (a blue curve in Figure 4b) and lower than that of the HFR-derived surface currents in the same frequency band [e.g., *Kim and Kosro*, 2013]. The rotational tendency of near-inertial currents becomes clockwise dominant offshore and reduced into rectilinear motions by equal clockwise and counterclockwise motions as it gets near the coast [e.g., *Pettigrew*, 1981]. Thus, the counter-clockwise near-inertial currents can appear in the coastal region of the northern Hemisphere. The persistent vortical features and eddies due to topography, shoreline, and riverine coastal waters may also generate the counter-clockwise currents. Additionally, the instrumental error may introduce the enhanced variance of currents in both rotations, which can reduce the SNR of counter-clockwise currents when the variance of counter-clockwise currents is dominantly lower than that of clockwise currents.

The maps of amplitudes of ROMS surface currents in the near-inertial frequency band (Figures 5a and 5b) exhibit a spatial structure similar to those of HFR-derived surface currents including amplitude PDFs and coastal inhibition (Figures 6a, 6d, and 6g). The counter-clockwise near-inertial flows appear to the north of

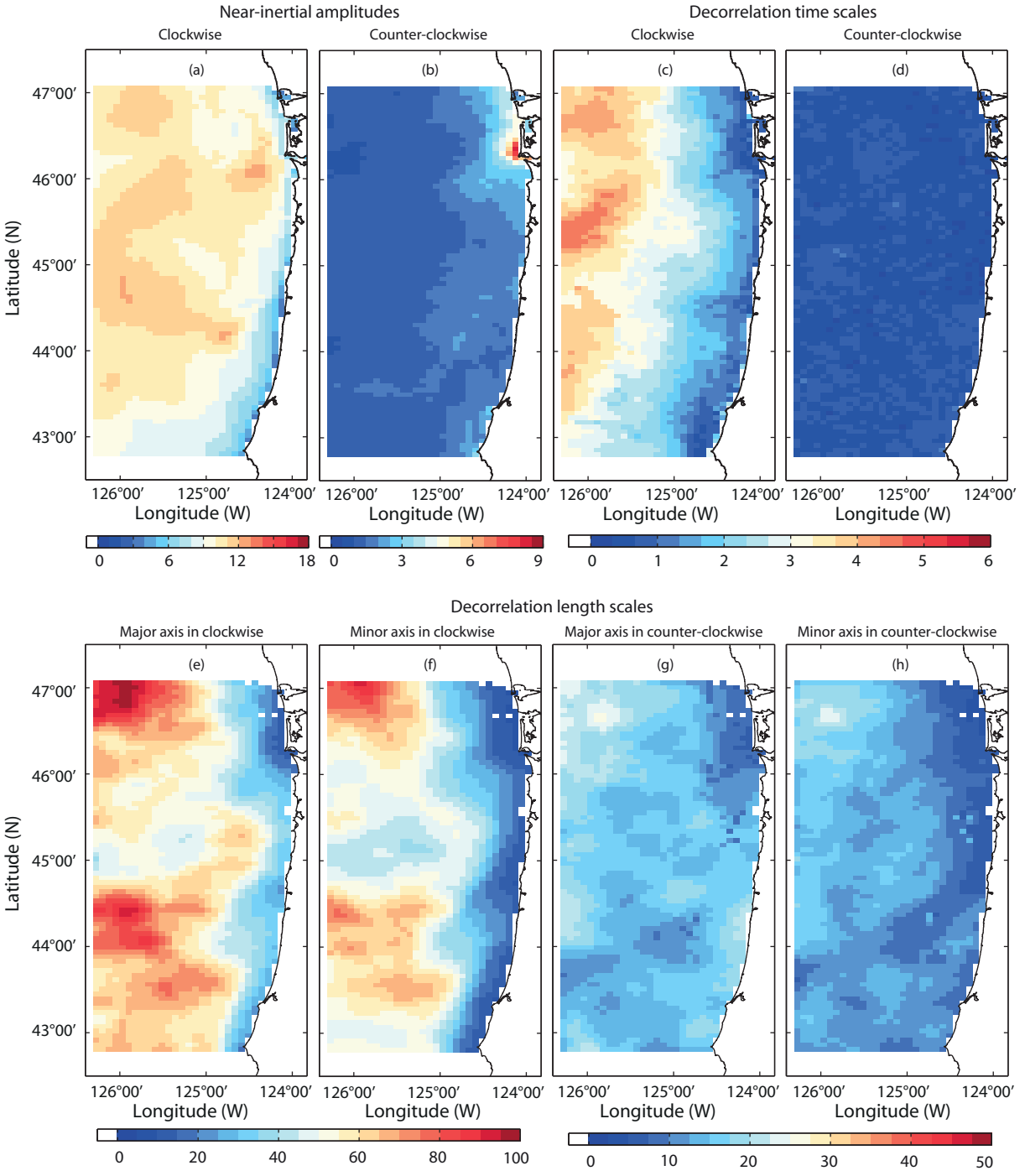

Figure 5. (a, b) Amplitudes (cm s^{-1}), (c, d) decorrelation time scales (days), and (e–h) decorrelation length scales (km) in the major and minor axes, estimated from ROMS surface currents in the clockwise and counter-clockwise near-inertial frequency bands. The identical analysis in *Kim and Kosro* [2013] was applied. Figures 5a and 5b correspond to Figures 2a and 2b in *Kim and Kosro* [2013], Figures 5c and 5d correspond to Figures 7a and 7b in *Kim and Kosro* [2013], and Figures 5e–5h correspond to Figure 10 in *Kim and Kosro* [2013].

the CR mouth for both ROMS and HFR surface currents (compare Figure 5b here and Figure 2b in *Kim and Kosro* [2013]), but these are much more subtle in the model than observations.

3.3.3. Decorrelation Time and Length Scales

The decorrelation time scales of ROMS surface currents in the near-inertial frequency band (Figures 5c and 5d) are close to those of HFR-derived surface currents (Figures 7a and 7b in *Kim and Kosro* [2013]). Their

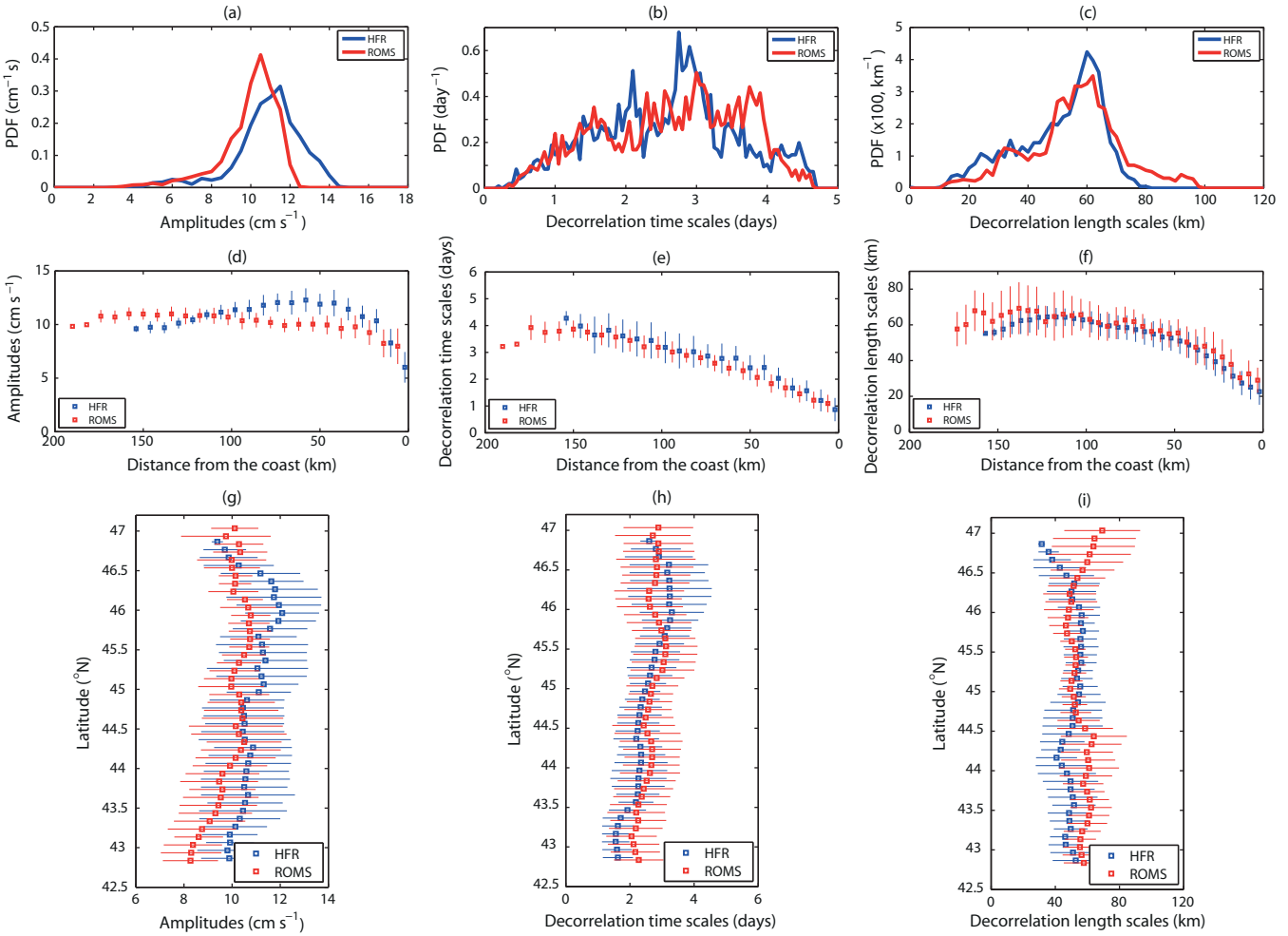

Figure 6. For the quantitative comparison between ROMS and HFR clockwise near-inertial surface currents, the probability density functions (PDFs) of their amplitudes (cm s^{-1}; left) (see Figures 2a and 5a in *Kim and Kosro* [2013]), decorrelation time scales (days; middle) (see Figures 5c and 7a in *Kim and Kosro* [2013]), and major axes of the decorrelation length scales (km; right) (see Figures 5e and 10a in *Kim and Kosro* [2013]). The PDFs are presented with (top) values in the entire study domain, (middle) the along-shore averaged values and their standard deviation as a function of distance from the coast, and (bottom) the cross-shore averaged values and their standard deviation as a function of latitude. The bin sizes are (a) 0.5 cm s^{-1}, (b) 0.05 days, (c) 2 km, (d–f) 8 km, and (g–i) 0.1°, respectively.

unconditioned PDFs and their along and cross-shore averaged PDFs show that more than 92% of individual estimates from HFR observations and ROMS outputs are matched within the errorbars (Figures 6b, 6e, and 6h).

The decorrelation length scales of ROMS near-inertial surface currents are very similar to those of HFR surface currents in terms of the order of magnitude and cross-shore structure including coastal inhibition (Figures 5e–5h) (see Figure 10 in *Kim and Kosro* [2013]). Their PDFs also exhibit the consistent distribution in the cross-shore direction and latitude (Figures 6c, 6f, and 6i).

The coherence of the observed wind at W2 and W3 with respect to the wind at W1 is shown in Figures 7a and 7b. The magnitude and phase of coherence depend on the distance between buoy locations [e.g., *Huyer et al*., 1975]. The phase at clockwise diurnal and semidiurnal frequencies shows that the land/sea breeze in the southern Oregon leads the one in the northern Oregon and Washington by about half an hour and one hour, respectively. The ratio of rotary spectra [$S_{W2}(\sigma)/S_{W1}(\sigma)$ and $S_{W3}(\sigma)/S_{W1}(\sigma)$] shows that subinertial winds have nearly the same spectral contents at different locations (Figure 7c). This ratio drops for higher frequency winds in both clockwise and counter-clockwise rotations.

Examples of the spatial structure of ROMS wind stress and surface currents in the near-inertial frequency band are presented with the magnitudes and phases of the spatial coherence with respect to

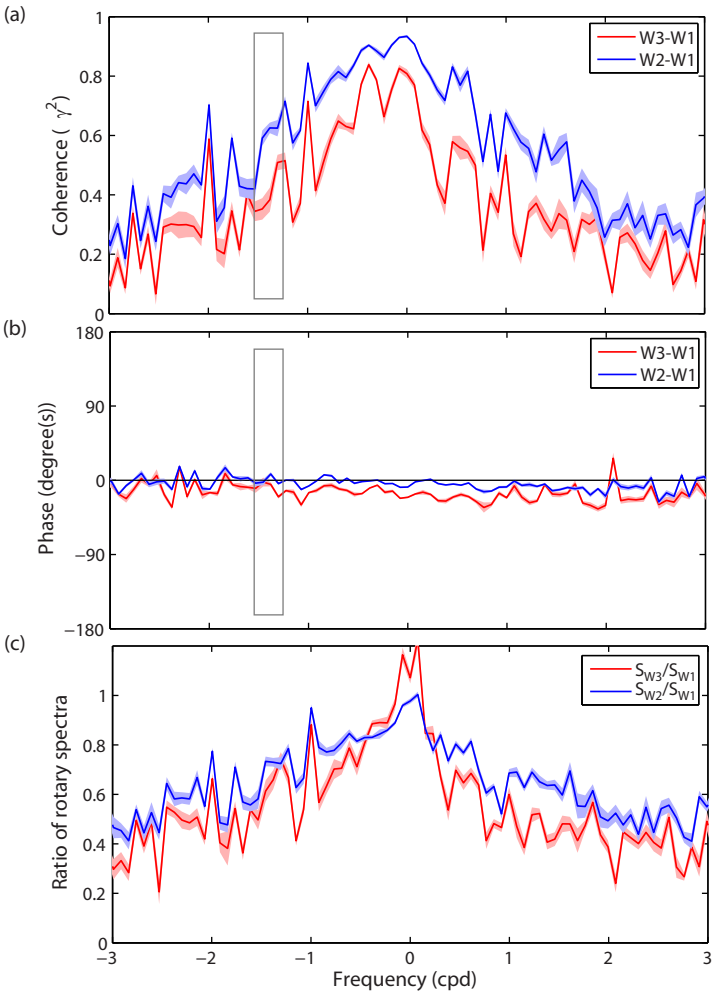

Figure 7. (a, b) Magnitudes and phases (degrees) of coherence and (c) the ratio of rotary spectra [$S_{W2}(\sigma)/S_{W1}(\sigma)$ and $S_{W3}(\sigma)/S_{W1}(\sigma)$] between the observed wind at W2 (NDBC 46029) or W3 (NDBC 46041) relative to the wind at W1 (NDBC 46050). Negative phases indicate that the reference wind (W1) leads the target wind (W2 or W3). The error bars are estimated with the Jackknife method. A black box in Figure 7a denotes the clockwise near-inertial frequency band.

four grid points (A, B, C, and D) (Figure 8). The zonal and meridional sections of magnitudes centered on those reference points are shown in Figure 9. The coherence and phase of ROMS wind stress in the near-inertial frequency band are consistent with the magnitudes of coherence between in situ wind data in the same frequency band. For instance, the magnitude of coherence between W1 and W2 is marked as E in Figure 9b. The decorrelation length scales obtained from long-term NDBC wind data off Oregon and northern California are in the range of 200–300 km [e.g., *Kim*, 2014], which is consistent with length scales computed from the model wind stress (e.g., Figure 9b).

The ROMS wind stress and surface currents in the clockwise near-inertial frequency band have decay shapes of Gaussian and exponential functions, respectively (Figures 8 and 9). The spatial coherence of the ocean surface currents is smaller (faster dropoff) than that in the wind stress, and the coherence for currents drops off faster near coast, compared with those father offshore (Figures 8b, 8f, 8j, 8h, and 9a–9d). The ROMS surface currents have similar length scales compared with those of the HFR surface currents (Figures 9c–9f).

4. A Statistical Model

In this section, we describe the transfer functions and response functions derived from observations and the numerical model outputs and compare these to each other and analytical models. Based on these analyses, a choice of an analytical model that best presents statistical model will be made.

A statistical model constructs a linear (or nonlinear) relationship between observed or model wind stress and currents in the frequency and time domains, which correspond to the transfer function and the impulse response function, respectively. Note that both wind stress and surface currents are analyzed using zonal and meridional components in order to keep a consistent directional convention and to avoid ambiguity in the veering angle and phase.

The transfer functions (or response functions) can differ in winter and summer [e.g., *Kim et al.*, 2010] as a result of seasonal stratification (e.g., due to seasonal difference in heat flux, mixed layer depth, and freshwater inputs from the CR). However, in this paper we will disregard any seasonal differences, which will be addressed instead in a future analysis.

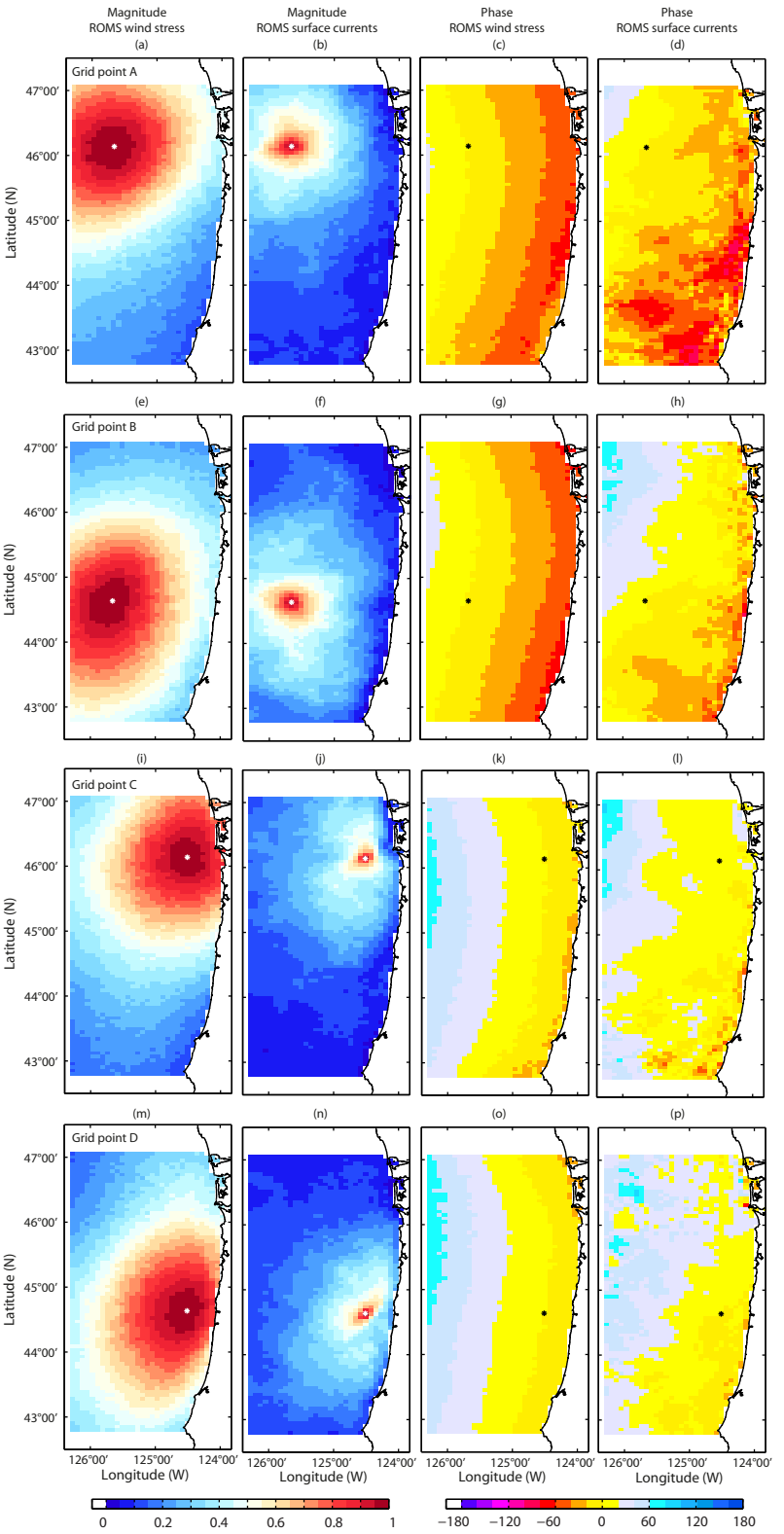

Figure 8. Magnitudes and phases (degrees) of the spatial coherence of ROMS wind stress (first and third columns) and ROMS surface currents (second and fourth columns) in the clockwise near-inertial frequency band relative to a reference location (A, B, C, and D in Figure 3b, marked with white or black stars). First and third columns: Magnitudes and phases of the spatial coherence of ROMS wind stress; Second and fourth columns: Magnitudes and phases of the spatial coherence of ROMS surface currents. The magnitude is the value averaged over the near-inertial frequency band, and the phase is the value at a single frequency bin. (a–d) Grid point A. (e–h) Grid point B. (i–l) Grid point C. (m to p) Grid point D.

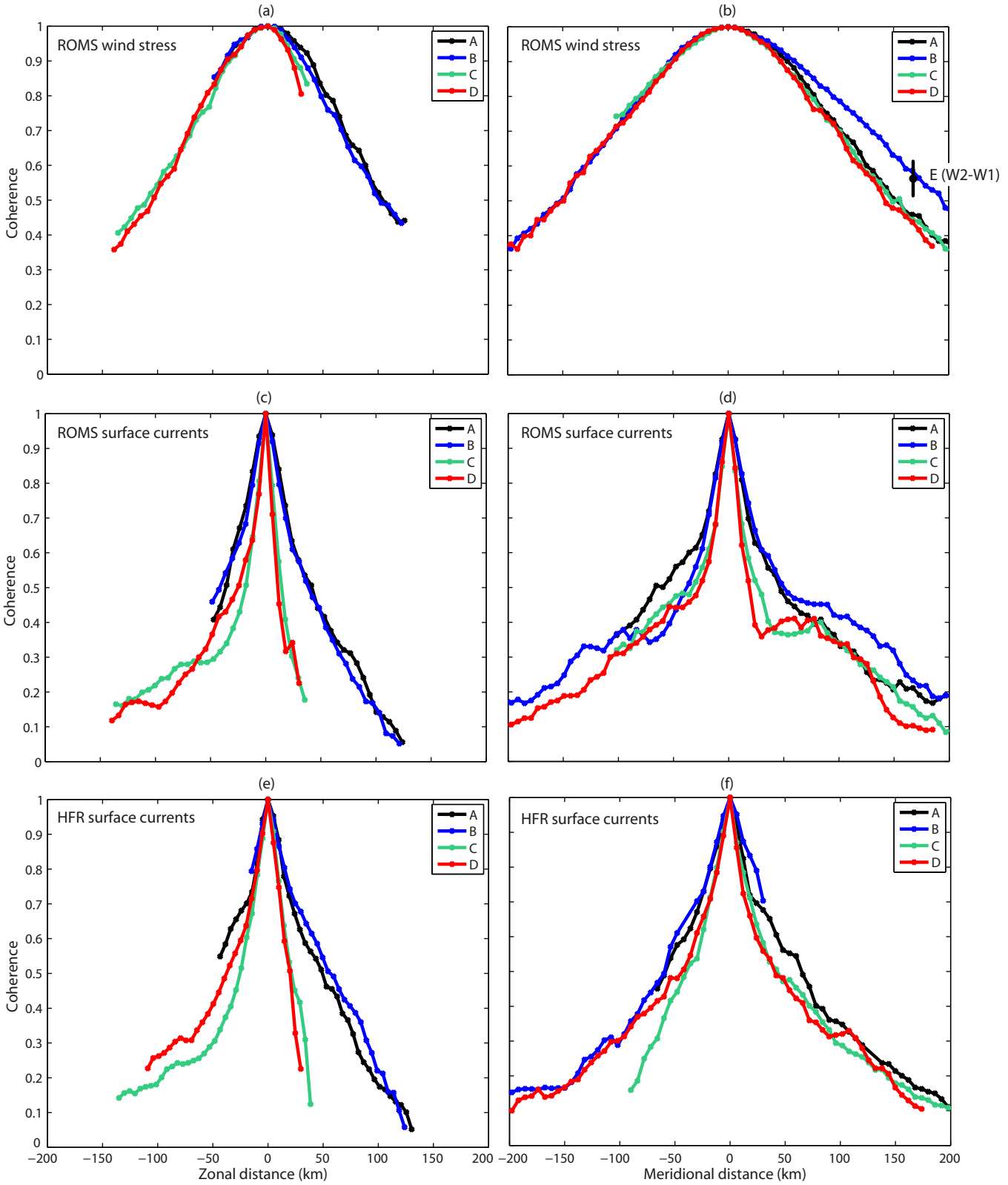

Figure 9. (a, c) Zonal and (b, d) meridional cross sections of Figure 8. (a, b) ROMS wind stress. E in Figure 9b indicates the magnitude of coherence between W1 and W2 in the clockwise near-inertial frequency band and its error bar (Figure 7a). (c, d) ROMS surface currents. (e, f) HFR surface currents.

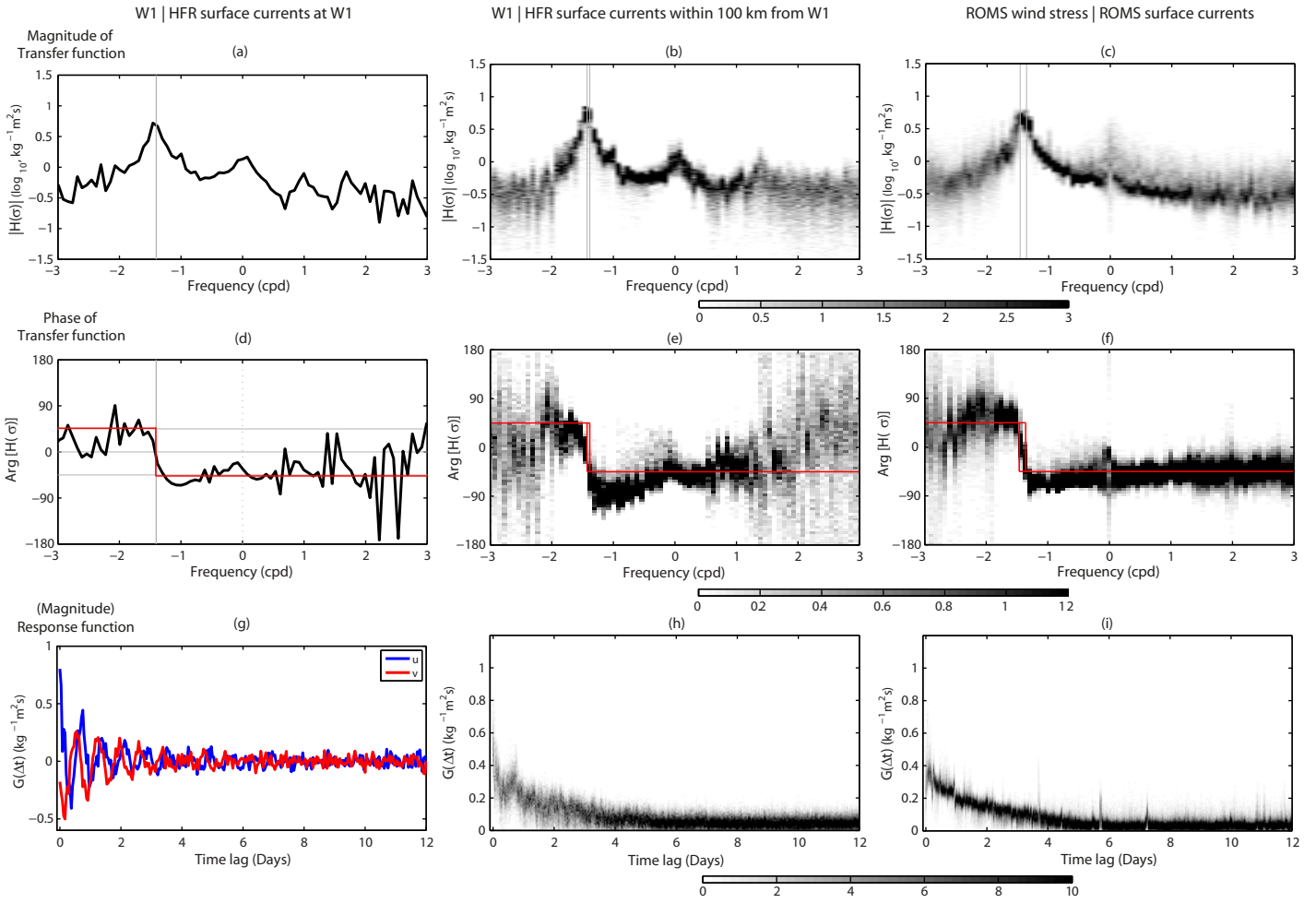

Figure 10. Wind transfer functions and response functions derived from wind stress at W1 and HFR-derived surface currents (left) at the nearest single grid point from W1 and (middle) at grid points within 100 km from W1, and (right) ROMS wind stress and ROMS surface currents at individual grid points. Subfigures in the right two columns (Figures 10b, 10c, 10e, 10f, 10h, and 10i) are presented as probability density functions (PDFs) at each frequency bin or time lag. (a–c) Magnitudes (kg^{-1} m^2 s) of transfer functions. (d–f) Phases (degrees) of transfer functions. (g) Response functions (kg^{-1} m^2) of the *u* component and *v* component. (h, i): PDFs of magnitudes of response functions at each time lag. The vertical solid gray lines in Figures 10a–10f indicate either the local inertial frequency or their range. The horizontal red lines in Figures 10d–10f indicate the phase of $\pm 45^\circ$.

4.1. Transfer Functions in the Frequency Domain

4.1.1. Broadband

As an example of the data-derived model, the transfer function and response function are computed from wind stress at the NDBC 46050 (W1) buoy and surface currents at the nearest single grid point from the W1 buoy (the left column in Figure 10) and at grid points within a 100 km radius from the W1 buoy (the middle column in Figure 10). The response function (Figure 10g) is obtained from the inverse Fourier transform of the transfer function (Figures 10a and 10d). To present estimates of the response functions and transfer functions at multiple grid points (middle and right columns in Figure 10) we use their PDFs at individual frequency bins or time lags.

The amplitude of the transfer function corresponding to the colocated wind and surface current time series has a peak and its phase changes abruptly at the clockwise inertial frequency ($f_c = -1.47$ cpd, Figures 10a and 10d). The peak at low frequency results from the geostrophic balance between the local pressure setup against the coast and currents [e.g., *Kim et al.*, 2009], which can not be included in the three one-dimensional analytical models (section 2). For colocated wind and surface current time series, the phase varies in a range of $\pm 45^\circ$ for -3 cpd $\leq \sigma \leq 1$ cpd, and its rapid variations are found at $\sigma \geq 1$ cpd (Figure 10d). The range of phases for -3 cpd $\leq \sigma \leq 1$ cpd is consistent with the ones obtained from the Ekman layer model at $z = 0 - 0.25\delta_E$, where δ_E is the Ekman layer depth, and the surface averaged Ekman model (Figures 1d and 1f) and differs clearly from $\pm 90^\circ$ suggested by the slab model (Figure 1b). Both amplitude and phase of the data-

derived transfer function are consistent with the ones reported in other coastal regions [e.g., *Kim et al.*, 2009, 2011]. The response function presents the near-inertial oscillations decaying within 3–5 days (Figure 10g).

The PDFs of transfer functions, using observed surface currents within 100 km of W1, show peaks at inertial and low frequencies and the phase shift at the inertial frequency (Figures 10b and 10e). The estimates at high frequency ($\sigma > 1.5$ cpd and $\sigma < -2$ cpd) are highly scattered. The phases range from 30° to -80° at the clockwise inertial frequency and continue to decrease to a range of -45° to -135° at the clockwise subinertial frequency, then keep nearly constant as $-45^\circ \pm 20^\circ$ in the rest of the frequency range except a hump at the zero frequency. The magnitudes of the time domain response functions exhibit patterns decaying within 3–5 days (Figure 10h) (see Appendix B for cautionary remarks on the auto-correlation analysis of self-similar time series).

The PDFs of transfer functions estimated from ROMS wind stress and surface currents are presented in Figures 10c and 10f. For this calculation, we utilized the wind stress at the same locations as the model currents in the subsampled domain, point-by-point. These point-by-point transfer functions show the variation in their peaks and phases comparable to data-derived transfer functions (left and middle columns in Figure 10). The decay time scales obtained from the model-derived response functions are also similar to observed ones (Figures 10g and 10h). The magnitude of the model-derived transfer function at low frequency ($|\sigma| \leq 0.1$ cpd) appears scattered compared with that of the data-derived transfer function, possibly, because of the difference in the spatial scale where the pressure gradients in the cross-shore direction are between the model and observations (Figures 10a–10c) [e.g., *Kim et al.*, 2010]. The phase transition of the model-derived transfer function at the inertial frequency is more steplike than that of the data-derived transfer function (Figures 10d–10f) and even better compared to $\pm 45^\circ$ pattern of the Ekman model than the data-derived transfer function. This possibly reflects the fact that the model wind stress and currents are sampled at the same point, while for observation-based estimates the time series of surface currents could be as far as 100 km from the wind data.

Comparing the data-derived transfer functions and three analytical models, the near-surface averaged Ekman model and the Ekman model have more similarity to approximate the data-derived model from HFR observations than the slab layer model. In addition, the near-surface averaged Ekman model has a better adaptivity as the averaging depth (z^*) can be used as a free parameter to fit the analytical model to the observations (see below). Note that the HFR-derived surface currents may be considered as the upper $O(1)$ m averaged currents.

4.1.2. Near-Inertial Frequency Band

The transfer functions estimated from (1) wind stress at individual wind buoys and HFR surface currents in their 100 km radius and (2) colocated ROMS wind stress and surface currents are presented with maps of their magnitude averaged over the near-inertial frequency band ($\hat{f}_c$) and phase at the local inertial frequency (f_c), corresponding to locations (Figure 11). As the phase varies within a circular range (0° to 360°, then 0°), its ensemble average may require some care in the analysis and interpretation. Particularly, as the phase of the transfer function within the near-inertial frequency band changes from positive to negative, a simple averaging of phases may not be a good estimator. Thus, we use the phase at the local inertial frequency. As the counter-clockwise near-inertial motions are very weak and may not have a direct dynamical relationship with wind stress, the only clockwise transfer functions are presented. The point-by-point transfer functions in the clockwise near-inertial frequency band can yield $O(200 - 300)$ km spatial scales of wind-coherent near-inertial surface currents, which turn out to be much broader than the length scales of total near-inertial surface currents (Figure 10 in *Kim and Kosro* [2013]).

The magnitude of transfer functions for a given wind buoy is the largest near the wind buoy and decays as a function of distance. The decorrelation length scale is generally larger in the alongshore direction (Figures 11a–11c). The model-derived point-by-point wind transfer functions (Figure 11d) may be useful to reveal a spatial bias in the transfer function estimated from the wind at a single buoy under the assumption of a uniform wind field. The phase maps of transfer functions in the clockwise near-inertial frequency band (Figures 11e–11g) have similar spatial patterns because they depend only on the phase differences in winds at different locations (W1, W2, and W3, Figure 7b).

The cross-validated wind skill (see section 5a in *Kim et al.* [2009] for the definition) indicates the fraction of clockwise near-inertial variance explained by the direct wind. It is shown using observed winds at individual buoy locations (Figures 12a–12c and 12e–12g), winds at the three buoys combined (Figures 12d and 12h), and the model wind stress at all points (Figure 12i). The data-derived and model-derived estimates are shown

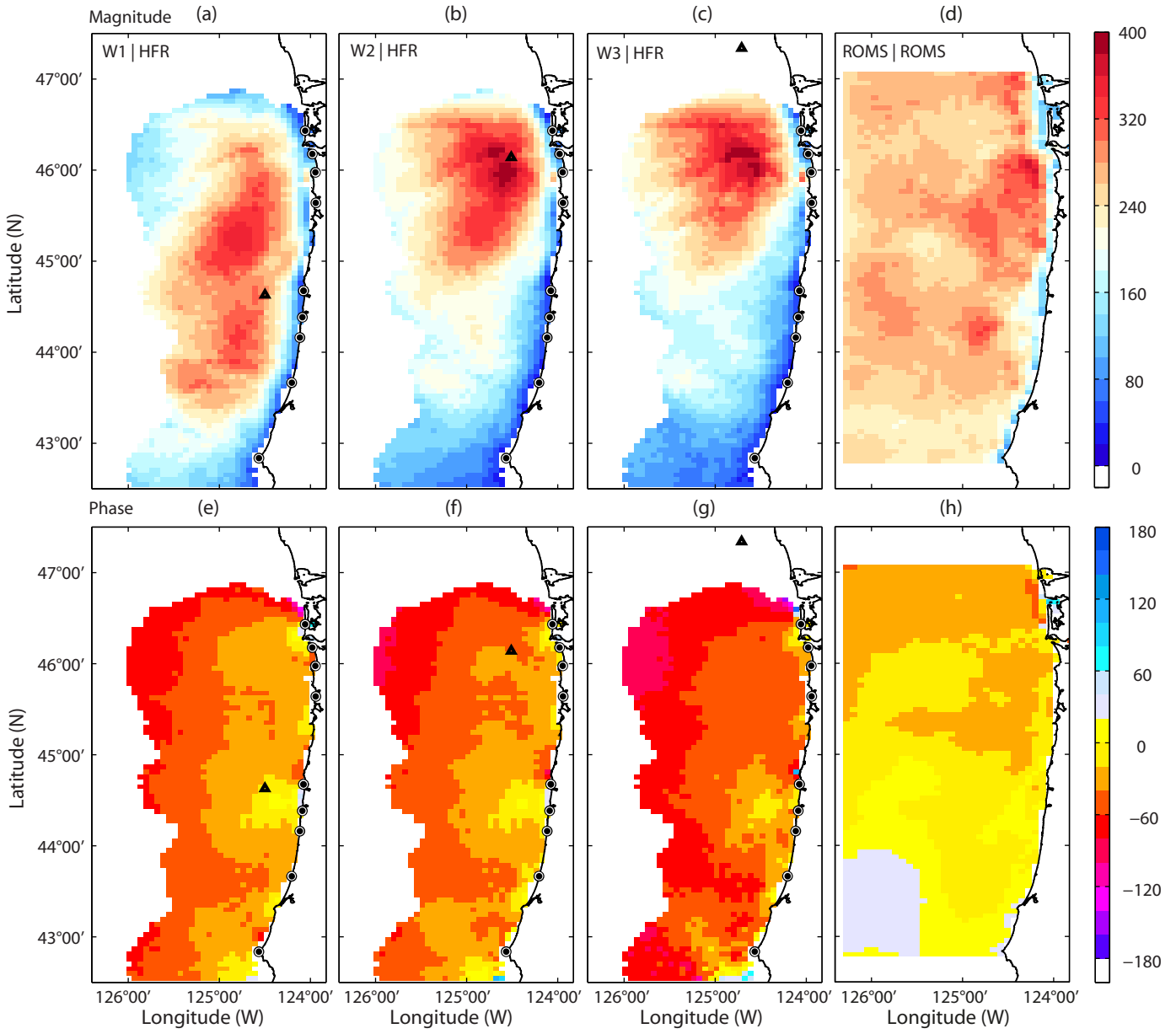

Figure 11. Magnitudes (kg^{-1} m^2 s) and phases (degrees) of transfer functions in the clockwise near-inertial frequency band. (a–c) and (e–g) Transfer functions are estimated with the wind data at a single location (a black triangle), i.e., spatially uniform wind field, and HFR-derived surface currents. (d, h) Transfer functions are estimated with ROMS wind stress, i.e., spatially varying wind field, and ROMS surface currents at individual grid points. The magnitude is the value averaged over the near-inertial frequency band, and the phase is the value at the local inertial frequency where surface currents are observed.

at the top and bottom of Figure 12, respectively. The skill is the largest near the wind buoy location and decreases with distance. For surface currents within a 100 km radius from the wind buoys, 25% to 45% of their near-inertial variance is directly coherent with locally available wind observations. Both wind skills at W2 and W3 have similar footprints (Figures 12b and 12c), and the wind skill at W3 is 30%–45% reduced compared with the skill by the wind at the W2 buoy because the common spectral contents of wind appear as the similar footprint and the distance to the study domain may affect the level of wind skill. The wind skill decreases markedly near the coast. About 40% of near-inertial variance can be explained with all three locally available observed wind data (W1, W2, and W3; Figure 12d).

The same analysis applied to the similarly sampled ROMS wind stress and surface currents exhibits the wind skills consistent with observations (Figures 12e–12h). The residual near-inertial variance may be initiated from remote areas or outside of the domain or could be due to noise in the fits or a model misfit.

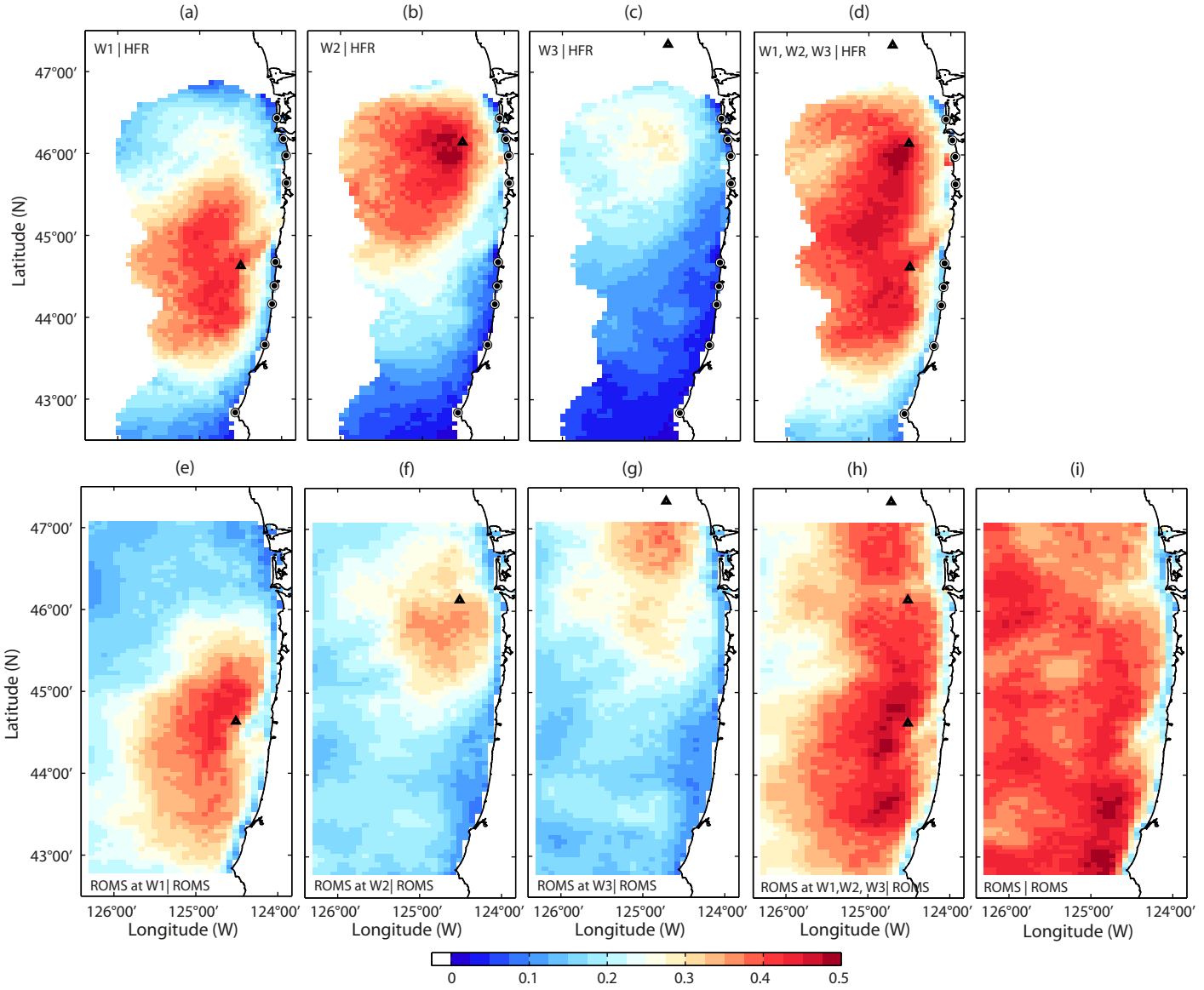

Figure 12. Cross-validated wind skill in the clockwise near-inertial frequency band. The transfer functions are estimated from (a–d) HFR surface currents and wind data at a single location of (a) W1, (b) W2, (c) W3, and (d) winds at the three buoys combined (W1, W2, and W3), (e–g) a single ROMS wind stress at individual locations of W1, W2, and W3 and ROMS surface currents, (h) ROMS wind stress at all locations of W1, W2, and W3 and ROMS surface currents, and (i) ROMS surface currents and ROMS wind stress at individual grid points. The locations of the wind(s) used in the skill estimated are marked as black triangles (only for Figures 12a–12h).

4.2. Response Functions in the Time Domain

To quantify the decorrelation time scales and other parameters of near-inertial motions, the data-derived response function (Figure 10e) can be fit to the analytical model-derived response functions (section 2). For illustration and comparison, the amplitudes of inertial motions in the slab layer model and the near-surface averaged Ekman model (equations (5) and (14)) are utilized here:

$$|\mathbf{G_S}(t)| = \frac{1}{2\rho h} e^{-rt}, \tag{17}$$

$$|\mathbf{G_E^*}(t)| = \frac{1}{\rho z^*} \mathrm{erf}\left(\frac{z^*}{\sqrt{4\nu t}}\right) e^{-rt}. \tag{18}$$

The parameters (z^*, ν, h, and r) are estimated to minimize the misfit between data-derived and analytical model-derived response functions. As the amplitude decays rapidly near zero time-lag and fluctuates at

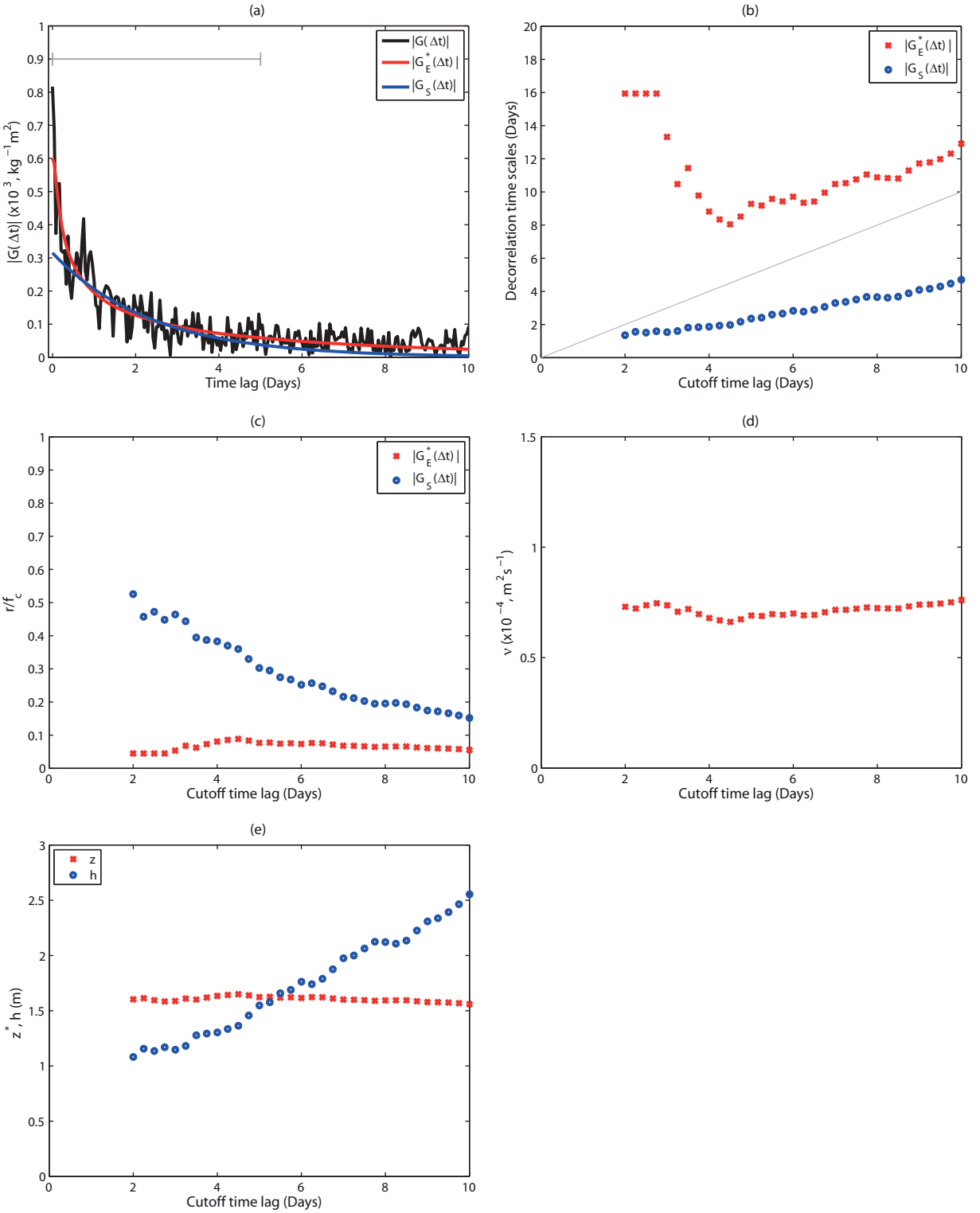

Figure 13. An example of the decorrelation time scale estimated from the magnitude of the response function in Figure 10. (a) The data-derived response functions are fitted with the near-surface averaged Ekman model ($\mathbf{G}_E^*$) and slab layer model ($\mathbf{G}_S$). The gray bar indicates the cutoff time lag. (b) Decorrelation time scales in terms of the cutoff time lag. The gray line indicates the one-to-one correspondence line which the time scale is equal to the cutoff time lag. (c) The ratio of the damping coefficient to the local inertial frequency (r/f_c). (d) Estimates of viscosity ($m^2\ s^{-1}$) from the near-surface averaged Ekman model. (e) Estimates of the slab layer depth (h) in equation (17) and the averaging depth (z^*) in equation (18).

higher time lags, the fitting is obtained over different intervals between 0 and l, where l is the cutoff time lag. The parameters (z^*, ν, h, and r) are estimated as functions of l. For instance, when the cutoff time lag is equal to 5 days ($l = 5$) (Figure 13a), the decorrelation time scales in the surface-averaged Ekman and slab layer models are given as $\lambda_E^* = 1/r = 8.5$ days and $\lambda_S = 2.5$ days, respectively (Figure 13b). As the initial time decay in the near-surface averaged Ekman model is dominated by the factor of $t^{-1/2}$, the secondary time decay factor ($e^{-rt} = e^{-t/\lambda_E^*}$) is estimated to be smaller than the factor ($e^{-rt} = e^{-t/\lambda_S}$) in the slab layer model (Figure 13b). Thus, the estimated decorrelation time scale ($\lambda_E^* = 8.5$ days) is longer than the length of time ($\sim$5 days) which takes for the response function to be reduced effectively. As mentioned above, the factor using parameter (λ_E^*) does not actually define the decay of the response function.

The ratio of the damping term to the local inertial frequency (r/f_c) is nearly constant as 0.1 for the near-surface averaged Ekman model and decreases from 0.5 to 0.2 for the slab layer model as the cutoff time lag increases (Figure 13c). The viscosity (ν) and the averaging depth (z^*) are nearly constant in near-surface averaged Ekman model (Figures 13d and 13e). The averaging depth ($z^* = 1.5$ m) obtained from fitting the data and model is close to the estimated averaging depth of HFRs [e.g., *Stewart and Joy*, 1974; *Fernandez et al*., 1996].

5. Summary

We investigated the characteristics of the directly wind-coherent near-inertial surface currents and the relevant analytical models to better capture the wind-current system, and the feasibility to reproduce the near-inertial signals using a coastal ocean model under space-limited in situ wind observations. Thus, we examined the data and ocean circulation model-derived transfer functions along with three one-dimensional analytical models in the frequency domain (e.g., slab layer, Ekman, and near-surface averaged Ekman models) to study the near-inertial surface currents directly coherent with local winds. The transfer functions and response functions, statistically estimated from (1) observed wind stress at NDBC buoys and high-frequency radar-derived surface currents and (2) ROMS wind stress and surface currents, isolate the directly wind-forced near-inertial surface currents, and they are used to compare with those derived from analytical models. The decorrelation time and length scales of directly wind-forced near-inertial surface currents are inferred with the decay time scales of the data-derived response function and the cross-validated wind skill, respectively. Their time scales are in a range of 3–5 days, and the length scales based on spatial wind skill are longer than 100 km. These estimates describe the highly coherent spatial structures of directly wind-forced near-inertial motions, separated from mixed near-inertial motions that may include the signal propagated from outside of the study domain.

The ROMS and observed near-inertial surface currents yield consistent results on amplitudes and decorrelation time and length scales in terms of the magnitude and their spatial distribution in the cross-shore direction and latitude.

The ROMS wind stress and surface currents obtained from a high-resolution forward ocean model are examined to derive point-by-point wind transfer functions. These model products have spatial structure and temporal decay scales similar to the observed near-inertial surface currents. Our comparisons confirm that the coastal ocean model reproduces essential features of near-surface near-inertial motions. Also, model-data comparisons show spatial scales on which data-derived transfer functions can be used, computed from in situ wind observations at a single location. The wind stress within a 100 km radius can be used as an effective driving force of the regional coastal circulation in the near-inertial frequency band.

The slab layer model requires that wind stress and currents should be out of phase within the mixed layer, and it employs a single damping coefficient to explain the time decay of inertial motions. These assumptions may be limiting in describing a statistical relationship between observed wind stress and surface currents. Thus, among the one-dimensional analytical models, the near-surface averaged Ekman model better explains the statistically derived wind-current system than other analytical models considered. As an indication of a rigid choice, fitting the data-derived response function to the near-surface averaged Ekman model retrieves an estimate of the integrated depth ($z^* = 1.5$ m) that is close to the averaged sampling depth of the HFR-surface currents.

Appendix A: Derivation of Response Functions

A1. Slab Layer Model

The response function in the time domain is inversely Fourier transformed as

$$\mathbf{G_S}(t)=\frac{1}{2\pi}\int_{-\infty}^{\infty}\mathbf{H_S}(\sigma)e^{i\sigma t}\mathrm{d}\sigma, \tag{A1}$$

$$=\frac{-i}{2\pi\rho h}e^{-if_c t}e^{-rt}\int_{-\infty}^{\infty}\frac{e^{t\theta}}{\theta}\mathrm{d}\theta, \tag{A2}$$

$$=\frac{1}{2\rho h}e^{-if_c t}e^{-rt}. \tag{A3}$$

The time integration of the response function becomes

$$\mathbf{S_S}(t)=\int_0^t\mathbf{G_S}(t')\mathrm{d}t' \ , \tag{A4}$$

$$=\frac{1}{\rho h(if_c+r)}\left[-1+e^{-if_c t}e^{-rt}\right]. \tag{A5}$$

A2. Ekman Model

The wind response functions calculated from linear momentum equations in the finite depth using two approaches – Fourier transform and Laplace transform – are identical.

A2.1. Response Function Using Fourier Transform

The transfer function ($\mathbf{H_E}$) in the frequency domain is converted into the response function ($\mathbf{G_E}$) in the time domain using the inverse Fourier transform;

$$\mathbf{G_E}(z,t)=\frac{1}{2\pi}\int_{-\infty}^{\infty}\mathbf{H_E}(z,\sigma)e^{i\sigma t}\mathrm{d}\sigma, \tag{A6}$$

$$=-\frac{ie^{-\frac{z^2}{4\nu t}}e^{-if_c t}e^{-rt}}{2\rho\sqrt{\pi\nu t}}\mathrm{erfi}\left[\frac{2t\sqrt{i\theta}+\frac{z}{\sqrt{\nu}}}{2\sqrt{t}}\right]\Bigg|_{-\infty}^{\infty}, \tag{A7}$$

$$=\frac{1}{\rho\sqrt{\pi\nu t}}e^{-\frac{z^2}{4\nu t}}e^{-if_c t}e^{-rt}, \tag{A8}$$

where $\mathrm{erfi}(x)=-i\mathrm{erf}(ix)$ $(x\in\mathcal{R})$.

The time-transient spiral in vertical is

$$\mathbf{u_E}(z,t)=\int_0^t\mathbf{G_E}(z,t')\mathrm{d}t'=\mathbf{S_E}(z,t)-\mathbf{S_E}(z,0) \ , \tag{A9}$$

$$=\frac{e^{z\sqrt{\frac{if_c+r}{\nu}}}(-1+\beta_1)+e^{-z\sqrt{\frac{if_c+r}{\nu}}}(1+\beta_2)}{2\rho\sqrt{\nu(if_c+r)}}\Bigg|_0^t, \tag{A10}$$

$$=\frac{\alpha_1(-1+\beta_1)+\alpha_2(1+\beta_2)}{2\rho\sqrt{\nu(if_c+r)}} \ , \tag{A11}$$

where

$$\alpha_1=e^{\pi(1+i)z/\delta_E} \ , \tag{A12}$$

$$\alpha_2=e^{-\pi(1+i)z/\delta_E} \ , \tag{A13}$$

$$\beta_1=\mathrm{erf}\left[\sqrt{(if_c+r)t}+\frac{z}{2\sqrt{\nu t}}\right] \ , \tag{A14}$$

$$\beta_2=\mathrm{erf}\left[\sqrt{(if_c+r)t}-\frac{z}{2\sqrt{\nu t}}\right] \ , \tag{A15}$$

and $\delta_E=\pi\sqrt{2\nu/(f_c-ir)}$.

A2.2. Response Function Using Laplace Transform

The indefinite integral of the Ekman spiral ($\mathbf{S'_E}$) is adapted from the equation (13) in *Lewis and Belcher* [2004],

$$\mathbf{S'_E}(z,t)=\frac{\alpha_1(1+\beta_1)-\alpha_2(1-\beta_2)}{2\rho\sqrt{\nu(if_c+r)}}. \tag{A16}$$

Note that the transfer function, response function, and time-transient spiral, computed from the Laplace transform, are indicated with a prime (′).

Then time-transient spiral in vertical becomes

$$\mathbf{u}'_{\mathbf{E}}(z,t)=\mathbf{S}'_{\mathbf{E}}(z,t)-\mathbf{S}'_{\mathbf{E}}(z,0), \tag{A17}$$

$$=\frac{\alpha_1(-1+\beta_1)+\alpha_2(1+\beta_2)}{2\rho\sqrt{\nu(if_c+r)}}\ , \tag{A18}$$

which is the same as equation (A11). The response function is derived in the same way, identical to equation (A8):

$$\mathbf{G}'_{\mathbf{E}}(z,t)=\frac{\partial\mathbf{S}'_{\mathbf{E}}(z,t)}{\partial t}, \tag{A19}$$

$$=\frac{1}{\rho\sqrt{\pi\nu t}}e^{-\frac{z^2}{4\nu t}}e^{-if_c t}e^{-rt}. \tag{A20}$$

A2.3. Finite Depth

In the finite depth, the transfer function could not be solved analytically using Fourier transform. However, *Krauss* [1972] derived the response function at the finite depth using Laplace transform:

$$\mathbf{G}(z,t)=\frac{1}{\rho\sqrt{\pi\nu t}}\sum_{n=-\infty}^{\infty}e^{-\frac{h^2}{\nu t}\left(1+n-\frac{z}{2h}\right)^2}e^{-if_c t}e^{-rt}\ , \tag{A21}$$

where the response function at infinite depth corresponds to the case of $n = -1$.

The transfer function averaged over the depth (h) is

$$\int_0^h\sum_{n=-\infty}^{\infty}e^{-\frac{h^2}{\nu t}\left(1+n-\frac{z}{2h}\right)^2}\mathrm{d}z=-\sqrt{\pi\nu t}\,\mathrm{erf}\left[\frac{1}{\sqrt{\nu t}}\left(h(n+1)-\frac{z}{2}\right)\right]. \tag{A22}$$

Appendix B: Cautionary Remarks on the Auto-Correlation Analysis of Self-Similar Time Series

In estimates of decorrelation time scales, the auto-correlation of a given time series can be used. However, the auto-correlation of self-similar time series may generate spurious decorrelation structures regardless of the shape of the decay pattern.

Park et al. [2009] showed that the estimate of decorrelation scales depends on the decay pattern of individual pulses (e.g., exponential or Gaussian shape), which can include the artifacts due to the correlation of self-similar time series. They concluded that the spatial scale of inertial amplitudes decaying with a Gaussian shape is equal to $\sqrt{2}$ times of the actual length scale, which contradicts with the results obtained from synthetic time series [see Appendix of *Park et al*., 2009 for more details]. We suggest that the individuals or the composite mean of self similar time series be fitted with any functions having a decay pattern in order to quantify the decorrelation (time) scales. If other dynamic variables (e.g., wind stress) are available, the statistically computed response function can provide the decorrelation scales as presented in this paper.

The auto-correlation of self-similar time series may generate spurious decorrelation structures regardless of the shape of the decay pattern. A self-similar time series is defined as a continuous time series having similar shapes of pulses or amplitudes of which statistics is non-Gaussian such as river flows, rain fall, and wind speed, and inertial amplitudes. We evaluate the auto-correlation of synthetic self-similar time series [$d(t)$]:

$$d^e(t)=\sum_{n=1}^{N}a_n^e b_n^e(t)=\sum_{n=1}^{N}a_n^e\exp\left[-\frac{|t-t_n|}{\lambda_n}\right]\ , \tag{B1}$$

$$d^g(t)=\sum_{n=1}^{N}a_n^g b_n^g(t)=\sum_{n=1}^{N}a_n^g\exp\left[-\frac{(t-t_n)^2}{\lambda_n^2}\right]\ , \tag{B2}$$

$$d^l(t)=\sum_{n=1}^{N}a_n^l b_n^l(t)=\sum_{n=1}^{N}a_n^l\left(\frac{t-t_n}{t_n-\beta}+1\right)\ , \tag{B3}$$

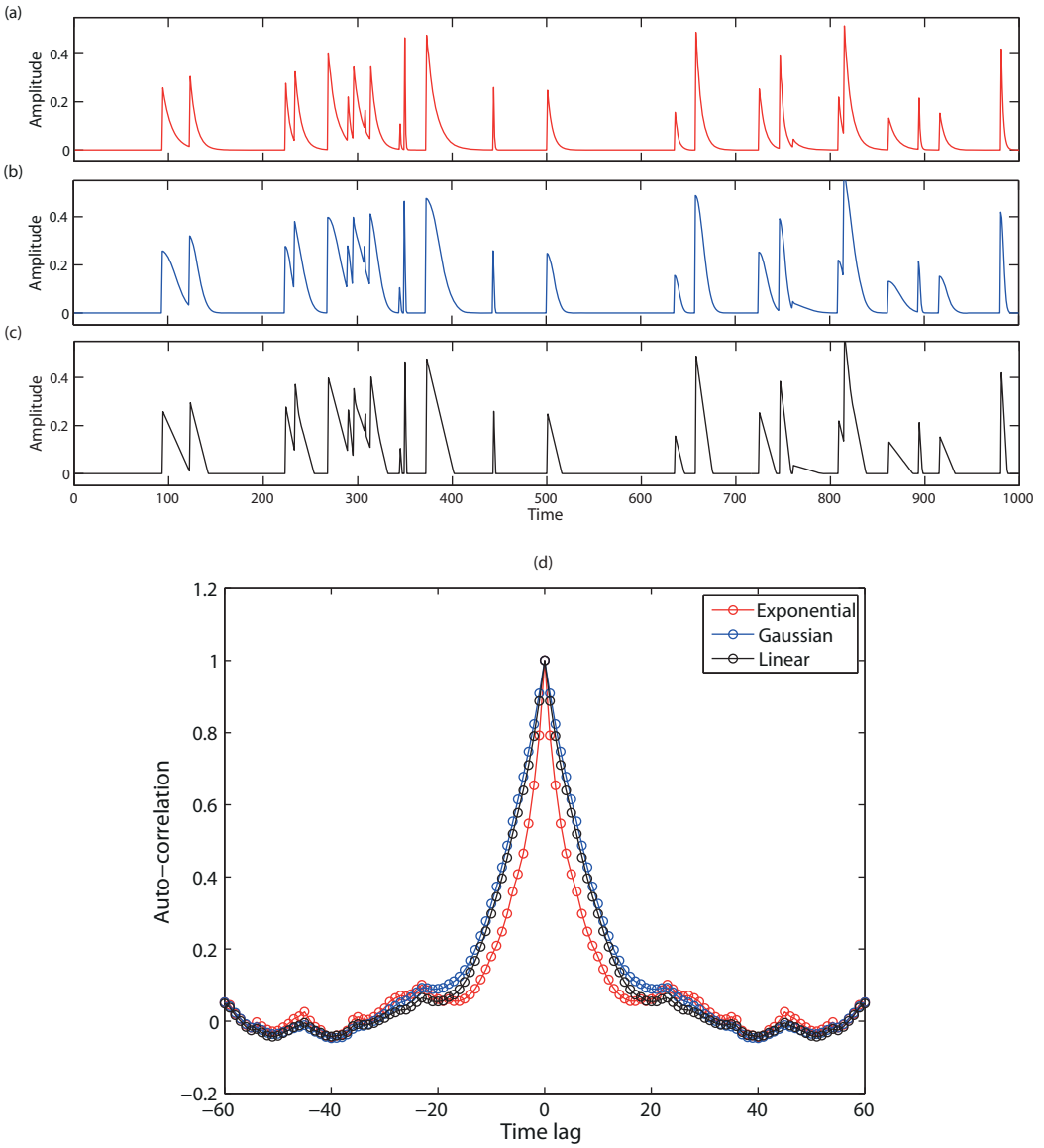

Figure B1. (a–c) Time series with multiple single-sided pulses which decay with the exponential, Gaussian, and triangle shapes. The amplitudes, decay coefficients, and timings are chosen as random variables. (d) Auto-correlations of time series given in Figures B1a–B1c.

where a is the independent amplitude at each t_n. λ is the decorrelation scale and β is a slope parameter of the triangle. Superscripts e, g, and l indicate the exponential, Gaussian, and triangle functions, respectively. Equations (B1)–(B3) are double-sided pulse time series, and the single-sided (positive only) pulse time series can be implemented as below,

$$d_n(t) = \begin{cases} d_n(t), & \text{if } t \geq t_n \\ 0, & \text{if } t < t_n. \end{cases} \tag{B4}$$

We generated the time series of multiple single-sided pulses that decay in the exponential, Gaussian, and triangle manner, respectively (Figures B1a–B1c). The amplitudes, decorrelation time scales, and timings of individual pulses were chosen as random variables. The auto-correlations of three sets of time series show the exponentially decaying shape regardless of the decaying pattern of the original time series (Figure B1d). Moreover, the number of pulses, the resolution of the time axis, decorrelation time scales, timings of pulses, and amplitudes did not change the shape of auto-correlation. The decorrelation time scale obtained from

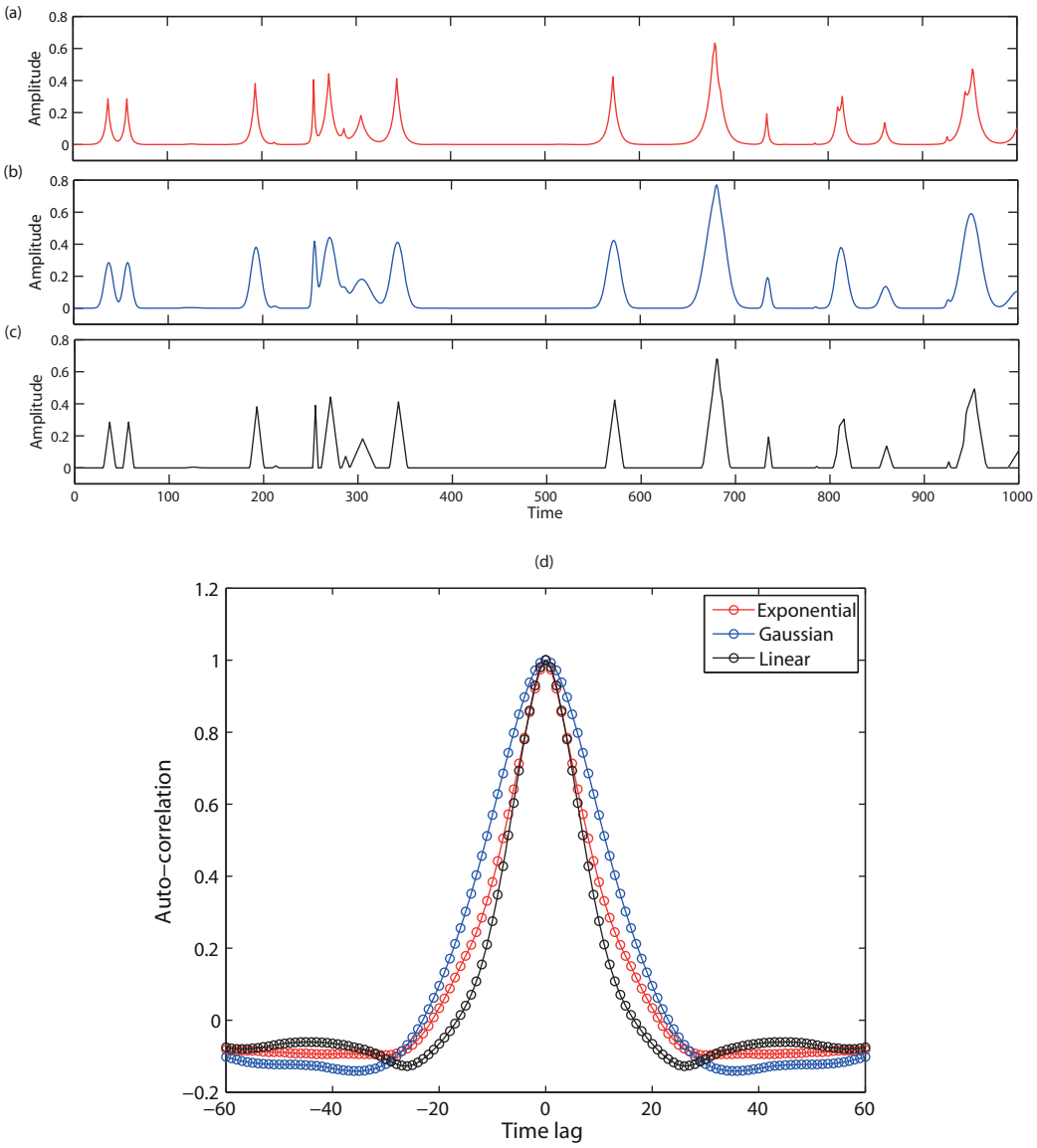

Figure B2. (a–c) Time series with multiple double-sided pulses which decay with exponential, Gaussian, and triangle shapes. The amplitudes, decay coefficients, and timings are chosen as random variables. (d) Auto-correlations of time series given in Figures B2a–B2c.

the auto-correlation does not have any relevance with decay scales of individual pulses. Thus, the decay scale of inertial amplitudes is nothing to do with $\sqrt{2}$ times of the actual length scale as described in *Park et al*. [2009]. In addition, the auto-correlation of double-sided pulses shows a Gaussian shape regardless of the decay pattern of the time series (Figure B2).

Acknowledgments

Sung Yong Kim is supported by the Basic Science Research Program through the National Research Foundation (NRF), Ministry of Education (NRF-2013R1A1A2057849), a program on the Human Resources Development of the Korea Institute of Energy Technology Evaluation and Planning (KETEP), Ministry of Trade, Industry and Energy (20134030200300), and a program on Management of Marine Organisms Causing Ecological Disturbance and Harmful Effects through Korea Integrated Marine Science Technology (KIMST) and Ministry of Fishery (MOF), Republic of Korea. P. Michael *Kosro* is supported by the National Science Foundation (NSF) (grants 0434810 and 0237710) and the National Oceanic Atmospheric Administration (NOAA) IOOS program (most recently NA11NOS0120036). Alexander L. Kurapov is supported by the NSF (grants OCE-0000734, OCE-0648314, and OCE-1030922), the Office of Naval Research Physical Oceanography Program (grant N000140810942), and NOAA (including CIOSS and IOOS-NANOOS). Surface current and wind data are provided by Oregon State University and National Data Buoy Center (NDBC), respectively. The data used in the paper will be available in a public repository to comply with the American Geophysical Union Publications Data Policy.

References

Alford, M. H. (2001), Internal swell generation: The spatial distribution of energy flux from the wind to mixed layer near-inertial motions, *J. Phys. Oceanogr.*, *31*, 2359–2368.

Barrick, D. E., M. W. Evans, and B. L. Weber (1977), Ocean surface currents mapped by radar, *Science*, *198*(4313), 138–144.

Crawford, G. B., and W. G. Large (1996), A numerical investigation of resonant inertial response of the ocean to wind forcing, *J. Phys. Oceanogr.*, *26*(6), 873–891.

Csanady, G. T., and P. T. Shaw (1980), The evolution of a turbulent Ekman layer, *J. Geophys. Res.*, *85*(C3), 1537–1547, doi:10.1029/JC085iC03p01537.

Daniault, N., P. Blouch, and F. Fusey (1985), The use of free-drifting meteorological buoys to study winds and surface currents, *Deep Sea Res., Part A*, *32*(1), 107–113, doi:10.1016/0198-0149(85)90020-2.

D'Asaro, E. A. (1985), The energy flux from the wind to the near-inertial motions in the surface mixed layer, *J. Phys. Oceanogr.*, *15*(8), 1043–1059.

Egbert, G. D., and S. Y. Erofeeva (2002), Efficient inverse modeling of barotropic ocean tides, *J. Atmos. Oceanic Technol.*, *19*(2), 183–204.
Ekman, V. W. (1905), On the influence of the Earth's rotation on ocean-currents, *Ark. Mat. Astron. Fys.*, *2*, 1–53.
Elipot, S., and S. T. Gille (2009), Ekman layers in the Southern Ocean: Spectral models and observations, vertical viscosity and boundary layer depth, *Ocean Sci.*, *5*, 115–139. [Available at http://www.ocean-sci.net/5/115/2009/.]
Emery, W. J., and R. E. Thomson (1997), *Data Analysis Methods in Physical Oceanography*, 634 pp., Elsevier, Boston.
Fairall, C. W., E. F. Bradley, D. P. Rogers, J. B. Edson, and G. S. Young (1996), Bulk parameterization of air-sea fluxes for tropical ocean-global atmosphere coupled-ocean atmosphere response experiment, *J. Geophys. Res.*, *101*(C2), 3747–3764, doi:10.1029/95JC03205.
Fernandez, D. M., J. F. Vesecky, and C. C. Teague (1996), Measurements of upper ocean surface current shear with high-frequency radar, *J. Geophys. Res.*, *101*(C12), 28,615–28,625, doi:10.1029/96JC03108.
Gonella, J. (1971), A local study of inertial oscillations in the upper layers of the ocean, *Deep Sea Res. Oceanogr. Abstr.*, *18*, 775–788, doi:10.1016/0011-7471(71)90045-3.
Gonella, J. (1972), A rotary-component method for analysis in meteorological and oceanographic vector time series, *Deep Sea Res. Oceanogr. Abstr.*, *19*, 833–846, doi:10.1016/0011-7471(72)90002-2.
Halliwell, G. R., Jr., and J. S. Allen (1987), The large-scale coastal wind field along the West Coast of North America, 1981–1982, *J. Geophys. Res.*, *92*(C2), 1861–1884, doi:10.1029/JC092iC02p01861.
Huyer, A., B. M. Hickey, J. D. Smith, R. L. Smith, and R. D. Pillsbury (1975), Alongshore coherence at low frequencies in currents observed over the continental shelf off Oregon and Washington, *J. Geophys. Res.*, *80*(24), 3495–3505, doi: 10.1029/JC080i024p03495.
Kim, S. Y. (2014), A statistical description on the wind-coherent responses of sea surface heights off the U.S. West Coast, *Ocean Dyn.*, *64*(1), 29–46, doi:10.1007/s10236-013-0668-3.
Kim, S. Y., and P. M. Kosro (2013), Observations of near-inertial surface currents off Oregon: Decorrelation time and length scales, *J. Geophys. Res. Oceans*, *118*, 3723–3736, doi:10.1002/jgrc.20235.
Kim, S. Y., B. D. Cornuelle, and E. J. Terrill (2009), Anisotropic response of surface currents to the wind in a coastal region, *J. Phys. Oceanogr.*, *39*(6), 1512–1533, doi:10.1175/2009JPO4013.1.
Kim, S. Y., B. D. Cornuelle, and E. J. Terrill (2010), Decomposing observations of high-frequency radar derived surface currents by their forcing mechanisms: Locally wind-driven surface currents, *J. Geophys. Res.*, *115*, C12046, doi:10.1029/2010JC006223.
Kim, S. Y., et al. (2011), Mapping the U.S. West Coast surface circulation: A multiyear analysis of high-frequency radar observations, *J. Geophys. Res.*, *116*, C03011, doi:10.1029/2010JC006669.
Kosro, P. M. (2005), On the spatial structure of coastal circulation off Newport, Oregon, during spring and summer 2001 in a region of varying shelf width, *J. Geophys. Res.*, *110*, C10S06, doi:10.1029/2004JC002769.
Krauss, W. (1972), Wind-generated internal waves and inertial-period motions, *Dtsch. Hydrogr. Z.*, *25*(6), 241–250.
Kundu, P. K. (1976), An analysis of inertial oscillations observed near Oregon coast, *J. Phys. Oceanogr.*, *6*, 879–893.
Kundu, P. K. (1984), Generation of coastal inertial oscillations by time-varying wind, *J. Phys. Oceanogr.*, *14*(12), 1901–1913.
Kundu, P. K., S.-Y. Chao, and J. P. McCreary (1983), Transient coastal currents and inertio-gravity waves, *Deep Sea Res. Oceanogr. Abstr.*, *30*(10), 1059–1082, doi:10.1016/0198-0149(83)90061-4.
Kunze, E. (1985), Near-inertial wave propagation in geostrophic shear, *J. Phys. Oceanogr.*, *15*, 544–565.
Lentz, S. J. (1995), Sensitivity of the inner-shelf circulation to the form of the eddy viscosity profile, *J. Phys. Oceanogr.*, *25*(1), 19–28.
Lewis, D. M., and S. E. Belcher (2004), Time-dependent, coupled, Ekman boundary layer solutions incorporating Stokes drift, *Dyn. Atmos. Oceans*, *37*, 313–351, doi:10.1016/j.dynatmoce.2003.11.001.
Madsen, O. S. (1977), A realistic model of the wind-induced Ekman boundary layer, *J. Phys. Oceanogr.*, *7*, 248–255.
McWilliams, J. C., E. Huckle, and A. F. Shchepetkin (2009), Buoyancy effects in a stratified Ekman layer, *J. Phys. Oceanogr.*, *39*(10), 2581–2599, doi:10.1175/2009JPO4130.1.
Mellor, G. L., and T. Yamada (1982), Development of a turbulence closure model for geophysical fluid problem, *Rev. Geophys. Space Phys.*, *20*(4), 851–875, doi:10.1029/RG020i004p00851.
Paduan, J. D., R. de Szoeke, and R. A. Weller (1989), Inertial oscillations in the upper ocean during the Mixed Layer Dynamics Experiment (MILDEX), *J. Geophys. Res.*, *94*(C4), 4835–4842, doi:10.1029/JC094iC04p04835.
Park, J., K. Kim, and R. Schmitt (2009), Global distribution of the decay timescale of mixed layer inertial motions observed by satellite-tracked drifters, *J. Geophys. Res.*, *114*, C11010, doi:10.1029/2008JC005216.
Perlin, N., R. Samelson, and D. Chelton (2004), Scatterometer and model wind and wind stress in the Oregon-northern California coastal zone, *Mon. Weather Rev.*, *132*(8), 2110–2129.
Pettigrew, N. R. (1981), The dynamics and kinematics of the coastal boundary layer off Long Island, Ph.D. thesis, Dep. of Meteorol. and Phys. Oceanogr., Mass. Inst. of Technol and Woods Hole Oceanographic Institution. [Available at http://hdl.handle.net/1721.1/27913.]
Pollard, R. T., and R. C. Millard (1970), Comparison between observed and simulated wind-generated inertial oscillations, *Deep Sea Res. Oceanogr. Abstr.*, *17*, 813–821, doi:10.1016/0011-7471(70)90043-4.
Price, J. F., and M. A. Sundermeyer (1999), Stratified Ekman layers, *J. Geophys. Res.*, *104*(C9), 20,467–20,494, doi:10.1029/1999JC900164.
Ralph, E. A., and P. P. Niiler (1999), Wind-driven currents in the Tropical Pacific, *J. Phys. Oceanogr.*, *29*, 2121–2129.
Samelson, R., P. Barbour, J. Barth, S. Bielli, T. Boyd, D. Chelton, P. Kosro, and J. Wilczak (2002), Wind stress forcing of the Oregon coastal ocean during the 1999 upwelling season, *J. Geophys. Res.*, *107*(C5), 3034, doi:10.1029/2001JC000900.
Shchepetkin, A. F., and J. C. McWilliams (2003), A method for computing horizontal pressure-gradient force in an oceanic model with a nonaligned vertical coordinate, *J. Geophys. Res.*, *108*(C3), 3090, doi:10.1029/2001JC001047.
Shchepetkin, A. F., and J. C. McWilliams (2005), The regional oceanic modeling system (ROMS): A split-explicit, free-surface, topography-following-coordinate oceanic model, *Ocean Model.*, *9*(4), 347–404, doi:10.1016/j.ocemod.2004.08.002.
Smith, R. L. (1968), Upwelling, *Oceangr. Mar. Biol. Ann. Rev.*, *6*, 11–46.
Stewart, R. H., and J. W. Joy (1974), HF radio measurements of surface currents, *Deep Sea Res. Oceanogr. Abstr.*, *21*, 1039–1049, doi:10.1016/0011-7471(74)90066-7.
Wang, Y., K. Hunter, and E. Bauerle (2001), Barotropic response in a lake to wind-forcing, *Ann. Geophysicae.*, *19*, 367–388, doi:10.5194/angeo-19-367-2001.
Weller, R. (1982), The relation of near-inertial motions observed in the mixed layer during the JASIN (1978) experiment to the local wind stress and to the quasi-geostrophic flow field, *J. Phys. Oceanogr.*, *12*, 1122–1136.
Weller, R. A., and A. J. Plueddemann (1996), Observations of the vertical structure of the oceanic boundary layer, *J. Geophys. Res.*, *101*(C4), 8789–8806, doi:10.1029/96JC00206.